Optimization of a Microfluidic Assay Computationally and Experimentally for Rapid and Sensitive Detection of Toxins in Water Samples

by

Hamid Aghamohammadi

A thesis
presented to the University of Waterloo
in fulfillment of the
thesis requirement for the degree of
Master of Applied Science
in
Electrical and Computer Engineering

Waterloo, Ontario, Canada, 2022

Author's Declaration

I hereby declare that I am the sole author of this thesis. This is a true copy of the thesis, including any required final revisions, as accepted by my examiners.

I understand that my thesis may be made electronically available to the public.

Abstract

Toxins are biological molecules observed in water resources, harmful to animal and human life. They are produced by certain algae and can find their way to the human body by drinking contaminated water, recreational water activities, or consuming contaminated crops or fish. Identification of these toxins in water resources becomes an essential part of the food industry and water quality analysis, creating an immediate need for an easy, portable, and rapid detection. Developing biosensors using immunological principles removes the need for complex and tedious analytical analysis while enabling sensitive and specific detection of biological molecules, such as toxins. The advent of microfluidic devices further simplifies the analysis and allows for rapid, automated, and in-field detection. The combination of biosensors with microfluidic devices preserves the advantages but overcomes the limitation of standard analysis methods.

The aim of this thesis is to first closely investigate the flow of the solution inside the microfluidic channel to develop a new computational model. Design and fabrication of microfluidic devices and implementation of immunoassay is a time-consuming process, and optimization of every aspect of the experiment is not feasible. A valid computational model can expedite the design and optimization process. In the next step, we showcased the use of the optimized microfluidic design for quick, in-field monitoring of cyanotoxins in water resources.

We present a novel bead-based competitive fluorescent assay using Quantum Dots (QDs) as a reporter agent for multiplexed detection of two types of toxins: Okadaic Acid (OA), a marine toxin, and Microcystin-LR (MC-LR), a freshwater toxin. To ease and automate the detection process, a reusable microfluidic device, Toxin-Chip, was designed and validated. It consists of (1) micromixer to mix and incubate the target toxin with the detection reagent, (2) detection chamber to magnetically retain beads for downstream analysis. The emitted signal from QDs captured on beads is proportional to the amount of toxin in the solution. An image recognition program was developed to carry out the signal read-out of microscopic images of the detection chamber. Two toxins were analyzed on the microfluidic chip, and the device exhibited a low limit of detection (LOD). The bead-based platform also showed remarkable chemical specificity against potential interfering toxins. The device's performance was tested and validated using natural lake water samples from Columbia Lake of Waterloo contaminated with cyanotoxins. The Toxin-Chip holds promise as a versatile and simple quantification tool for multiplexed field-based cyanotoxin detection, with the potential of extension for the simultaneous detection of more targets.

Acknowledgements

I would take this opportunity to thank the people who supported me through my journey to complete this research work and thesis.

I am grateful to Professor Mahla Poudineh for giving me the opportunity to work under her mentorship and for her continuous support and guidance in my studies. Her smart inputs, excellent guidance and constant encouragement, helped me immensely during my research and writing of the thesis. Her accompaniment was a precious credit to my career and professional development, and I could not have imagined having a better advisor.

I would like to thank Professor Alexander Wong and the Blue Lions Lab company, including Jason Deglint and Katie Thomas, for their collaboration and support during my master's. They trusted me and gave me the freedom to explore my ideas. My appreciation and thanks are also extended to the committee members, Prof. Nima Maftoon and Prof. Sushanta Mitra, for taking the time to read my thesis and their valuable suggestions.

Special thanks to the University of Waterloo for its financial support. I would like to acknowledge the National Science and Engineering Research Council of Canada (NSERC) for funding this research.

Lastly, I would send my deepest gratitude to my lovely family. I am standing on the shoulders of a supportive family, encouraging me to pursue my dreams. My parents, brother and sisters would remain the spirit for all success in my life.

Dedication

To my beloved

Mom and Dad...

Table of Contents

List of Figures

List of Tables

List of Abbreviations

D_a Damkohler number 19

BSA bovine serum albumin 27, 46

cAbs capture antibody 2, 3, 9, 10, 14, 18–21, 23, 24, 46, 47

CYN Cylindrospermopsin xii, 7, 36, 37, 46

dAbs detection antibody 2, 3, 20, 23, 46, 47

ELISA Enzyme-Linked Immunosorbent Assay x, xi, 1–4, 7, 19, 20, 23, 27–29, 31, 41

HABs Harmful algal blooms 5, 6

IgG immunoglobulin G x, 14, 20–25, 46, 47

LC-MS liquid chromatography combined with mass spectrometry 1, 41

LOD limit of detection iii, 3, 34, 41, 47

MC-LR Microcystin-LR iii, xi, xii, 6–8, 28, 29, 31–37, 39, 41, 46, 47

mcAb monoclonal capture antibody xi, 27–29, 31, 34, 46

OA Okadaic Acid iii, xi, xii, 6–8, 28, 29, 34–37, 39, 41, 46, 47

pAb polyclonal antibody 27

pAb-QDs polyclonal antibody conjugated with Quantum Dot xi, xii, 27, 28, 31, 33–36, 46

PDMS poly-dimethylsiloxane 19, 31, 43, 44

QDs Quantum Dots iii, 6, 8, 27, 36, 41, 45

STX Saxitoxin xii, 36, 37, 46

Chapter 1

Introduction

1.1 Immunological Detection Assay

The study of mechanisms in nature, particularly the human body, has inspired scientists to develop methods capable of investigating a biological medium in search of particular molecules. The information obtained from this biomolecule monitoring helps identify the targeted biological samples. This oriented and interdisciplinary study has brought tremendous advancements in the medical, environmental, and food industries. Traditional analytical techniques of monitoring biomolecules primarily use high-performance liquid chromatography combined with mass spectrometry (LC-MS) and ELISA [1]. In these methods, biological samples are collected and shipped to the centralized laboratory, where skilled personal use expensive and complicated equipment to analyze the samples. The results are usually reported after several days, which limits the reactive decision-making and dramatically hinders the application of these methods for an easy, fast, and in-field analysis. Massive effort and focus have been put into developing a quicker and more accessible approach for monitoring biomolecules. The principle of ELISA assay is based on specific antigen-antibody reaction providing a simple method for screening biomolecules. However, the ELISA methods suffer from low sensitivity and lack of specificity[2] compared to the instrumental assays[3].

1.2 ELISA

In general, different types of ELISA have been designed and implemented for detection of the target of interest. Here, I will elaborate on two kinds of ELISAs, which will later be used toward achieving my thesis's objective.

1.2.1 Sandwich ELISA

Sandwich ELISA has emerged as a robust, reliable clinical diagnostic and research tool. In these assays, target proteins are detected based on the specific interaction between a target antigen and capture antibody (cAbs) and detection antibody (dAbs) where the target antigen is "sandwiched" between cAbs and dAbs.

Due to the use of two specific antibodies in the sandwich ELISA, the risk of cross-reactivity is reduced, eliminating the necessity for a purification step in the analysis. The main disadvantage of a sandwich ELISA rise from its usage of matched pairs of capture and detection antibodies. They bind to different epitopes on the antigen and can be challenging to produce and validate to operate together. A sandwich ELISA is also more time-consuming and expensive compared to conventional ELISA[4].

1.2.2 Competitive ELISA

The competitive ELISA technique has proven to be effective in detecting small molecules at low concentrations that cannot be effectively captured through other ELISA types. In a basic competitive immunoassay, the targets of interest are conjugated on the sensing surface and compete with the target analyte in the solution to occupy the antibody binding sites. The binding is transduced into a detectable signal, measured, and correlated to the target concentration in the sample.

Competitive ELISAs can measure a more extensive range of antigens in a sample than a sandwich ELISA. This method does not use two epitopes on the target, which makes them more efficient in detecting small molecules that do not have multiple epitopes (for example, toxins). However, the complicated process of competitive ELISAs does not allow for higher specificity in the assay[4].

1.3 Bead-Based ELISA

Novel ideas have been integrated to improve the efficiency of ELISA assays. The incorporation of micro- or nanobeads, an alternative to a planar microarray, provides several advantages, such as (1) reducing the sample volume, (2) decreasing the incubation time, (3) improving the LOD, and (4) facilitating assay integration[5]. Bead-based sandwich assays are highly specific and easily integrable with the detection method. In this type of assays, micro- or nanosized particles are usually coated with the cAbs s and incubated with the sample solution that contains a target of interest. Then a specific dAbs and a reporter molecule are used to visualize the captured analytes[6].

The bead-based assays have been successfully utilized for different applications, such as early detection of coronavirus disease (COVID-19)[7], the infectious disease caused by the most recently discovered coronavirus; sepsis[8], a systemic response to infection[9]; malaria disease[10]; multiplex cytokine detection of ovarian cancer[11]; and detection of extracellular vesicles from whole blood for early-stage cancer diagnosis[12].

1.4 Biosensors

Biosensors are integrated devices using biorecognition components (aptamer, antibody, enzyme, etc.) and transduction elements (electrical, optical, etc.) to deliver quantitative analytical data. The operation of biosensors can be divided into three steps: interaction of the receptor with the sample, signal generation, and signal interpretation. The physical interaction of the target analyte with the bioreceptor is converted to a measurable signal by the transducer. This generated signal can be of various natures such as optical (fluorescence), electrochemical (redox), and electronic (resistance) and is subsequently measured and interpreted within the biosensing system. The involvement of biological entities like antibodies, DNA, proteins, and enzymes in the detection process sets biosensors apart from other sensor types[13], and they can detect a wide range of biological targets in environmental studies, biomedical and food industries, microbial detection, etc.

This emerging technology can facilitate the ELISA assay performance by providing a reacting site designed to respond to a specific antigen in the medium. Biosensors offer more accessible techniques for performing immunoassays and detecting the subsequent signal of interaction between biological molecules bringing a significant advancement to the analytical process. They allow relatively rapid, simple, and low-cost analysis while preserving the specificity of traditional analytical methods. This interdisciplinary field involves the collaborative efforts of biology, chemistry, engineering, physics, chemistry, and biotechnology.

The design of biosensors varies in the immunoreaction type (direct, sandwich, competitive etc.), detectable signal (optical, surface plasmon resonance, electrochemical etc.), reacting surface (wells, arrays, microbeads etc.), which is employed to tailor a sensor to its designated application

1.5 Microfluidic Technology

Although biosensors offer a highly sensitive detection, they consist of multiple analytical steps to be completed in laboratories by qualified personnel, hindering the automated and straightforward operation. Microfluidic technology has a very high potential to overcome these challenges since it allows for precise control of fluids, reduced consumption of expensive reagents, rapid isolation with high quality and throughput, portability, and low cost[14, 15]. From the operational standpoint, microfluidic devices integrate all conventional (mixing, washing, enrichment) analysis steps and are automated, portable, and user-friendly[16]. Moreover, the network of miniaturized microfluidic channels offers the benefit of having a multiplex study where many biosensors are implemented in the device and provide a more comprehensive analysis of the biological sample during a single run. Due to these advantages, microfluidic techniques offer improved performance over conventional bench-top systems and are increasingly used in biomedical analyses[17, 18].

1.5.1 Micromixers

Much effort has been focused to overcome performance limitations in the microfluidic devices, one of which is slow reagent mixing. The laminar flow regime inside microfluidic device hinders efficient mixing and reaction of the biological elements. Micromixers are powerful solutions toward addressing the inefficient mixing in microfluidic systems by inducting chaotic flow[19]. These mixers influence the flow inside the microchannels by incorporation of moving parts (stirring, shaking), energy inputs (acoustic wave, dielectrophoresis), or channel design (twisted channels, patterned channels). A fluorescence sandwich immunobead-based assay integrated with micromixers has been recently developed for the real-time continuous detection of glucose and insulin in live animals. The central to this technology, called real-time ELISA, is the capture of analytes on the microbeads and inside a chaotic microfluidic mixer in less than 1 minute, enabling real-time measurement[20]. The ELISA assays have been recently combined with micromixers and customized for various applications. However, device design and process optimization to achieve the best performance remain a substantial technological challenge.

1.5.2 Computational Model of Micromixer

Despite all the advancements in fabrication and designing of new and efficient microfluidic mixing devices, the field lacks a comprehensive study that explains the theory and mechanisms. Previously developed models investigated different aspects of binding analyte molecules to the reactive surface in bulk medium (not microfluidic platforms). For example, the interaction between analytes and antibodies was extensively studied on surface-based sensors[21, 22] or bead surfaces[23]. A mathematical model was developed for modeling the magnetic immunobead-based assay but considered only a simple situation of irreversible heterogeneous binding[24]. Other models studied coating of magnetic particles using random sequential adsorption theory[25], antigen capture using simple Langmuir kinetics[26], and motion of the magnetic particles under the influence of external magnetic fields using computational fluid dynamics[27]. More recently, a more detailed and accurate model examined the building blocks of immunoassays, including heterogeneous binding of analyte molecules on bead or sensor surfaces, attachment of bead labels to sensor surfaces, and generation of electrochemical current by bead labels[28]. To the best of our knowledge, there is no model that exploits immunobead-based assays integrated with microfluidic mixing. Such a model will be very beneficial as it systematically guides to design devices and assays with the best performance.

Herein we explore the complicated bead-based immunoassay and introduce a computational model that enables the rational design and optimization of the immunobead-based assay in a microfluidic mixing channel. We use numerical methods to examine the effect of the flow rates, channel geometry, bead's trajectory, and the analyte and reagent characteristics on the efficiency of analyte capture on the surface of microbeads. This model accounts for different bead movements inside the microchannel, intending to simulate an active binding environment. The model is further validated experimentally where different microfluidic channels are tested to capture the target analytes. Our experimental results are shown to meet theoretical predictions.

1.6 Toxins Contamination of Water Resources

Harmful algal blooms (HABs) are environmental pollution due to the release of toxins into water supplies. They have caused global hazards to aquatic organisms in the marine ecosystems and posed a severe threat to human health by contaminating water resources[29, 30]. The HABs are increasing in frequency, severity, and duration with anthropogenic effects, such as agricultural run-off, urban waste, manufacturing of detergents, and global

warming[1, 31].

1.6.1 Toxin Types and Regulations

MC-LR and OA are the two main products of HABs[32, 33]. MC-LR is the most common and toxic freshwater toxin produced mostly by cyanobacteria algae[34], while OA is a major marine neurotoxin produced by several species of dinoflagellates and has been found in both marine sponges and shellfish[35]. Both MC-LR and OA have been found to promote tumour growth and immunotoxic effects[36, 37]. World Health Organization has proposed 1 μg/L of MC-LR as a safety guideline for drinking water[38], and firmer limits ($\leq$ 0.3 μg/L) have been implemented by the U.S. Environmental Protection Agency [39]. Other emerging toxins have yet to be identified in detail; nonetheless, based on the information from different studies, consumption of 50 µg/person of OA can cause human illnesses[40].

1.6.2 Toxin as a Target Biomolecule

Biological toxins are the subject of extensive studies in the field of biosensors. Many biosensors have been developed to replace the conventional analytical method of water analysis. Their implementation is promising to meet the necessity of having a rapid, in-filed, and simple detection.

In a pioneering biosensor, MC-LR antibody immobilized on the graphene sheets and nanoparticles conjugated with secondary antibody formed a sandwich immunoassay to detect MC-LR[41]. In another assay, MC-LR was immobilized on the surface of graphene film and competed with target MC-LR in binding to monoclonal antibodies. The method constructed a signal-off competitive assay by monitoring the electron-transfer resistance changes of the electrodes[42]. In another biosensor, probes conjugated with QDs were integrated into an indirect competitive immunoassay for MC-LR detection[43]. QDs s improve the optical sensor's sensitivity toward small toxin molecules due to their unique optical properties. They offer higher brightness, resulting in a greater signal-to-background and their extreme photostability allows for continuous observation of biological events over prolonged periods of time[44]. In a recent study, an innovative DNA probe was developed by combining an MC-LR aptamer loop and a double-strand stem combined with copper nanoclusters, producing fluorescence signals[45]. Upon the addition of target MC-LR, the aptamer prefers binding to the target, which leads to a conformational change and quenching of the fluorescence signal produced by the probe. The optical sensors are useful in the development of a multiplex biosensor that can detect several targets at the same time.

Nanoparticles with different colors have been employed for the simultaneous detection of OA and MC-LR[46]. Upon target introduction, the quencher strands are released, causing the fluorescence signal to be emitted.

1.6.3 Microfluidic Sensors for Toxin Detection

Various groups have utilized microfluidic devices for developing toxin detection sensors. A portable fluorescence competitive immunoassay developed for simultaneous detection of Microcystin and CYN. The system uses a microarray loaded with reagents, cartridge, and custom software for quantifying the fluorescence images[47]. In another study, a microfluidic device with reagent columns was developed to monitor three cyanotoxins in parallel. In this device, the multiple steps of the bead-based competitive ELISA were controlled by integrated valves[48]. Recently, a group combined an integrated microfluidic device with a smartphone imaging module in which the operation steps were automated, and the smartphone-based detection facilitated in-field detection[49]. Similarly, four major toxins were detected simultaneously using a microfluid chip and an image analysis program where the sample was loaded in the center of the device connected to five reaction wells loaded with dried reagents[50].

The mentioned microfluidic assays are considered an advancement in the toxin detection field; however, they possess several limitations, including the devices are not re-usable, fully portable, continuous, and usually require complicated process (Table 4.1).

1.7 Thesis Objectives and Overview

This thesis aims to investigate the flow dynamic and formulization of sample and reagent mixing and reaction inside microfluidic channels to provide a strong optimization tool and shorten the tedious process of microfluidic device optimization. We developed a computational model to address this challenge and validated its ability to simulate intricate channel and immunoassay with experimental results.

Next, the optimized design was utilized to develop a novel biosensor for rapid detection of biological toxins in water samples. We designed and optimized a novel immunoassay and implemented it in an automated microfluidic device enabling fast and in-field analysis. We demonstrated the capability of this novel design with various experiments, including lake water sample analysis.

The remainder of this thesis will be organized as follows:

1.7.1 Chapter 2: Computational and Experimental Model to Study Immunobead-Based Assays in Microfluidic Mixing Platforms

This chapter presents an integrated three-dimensional (3D) computational and experimental model that investigates the immunobead-based assays inside microfluidic mixing devices. We studied the effect of diffusion and convection on the analyte movement inside a simple microfluidic channel. The impact of different patterns of bead movements and different numbers and sizes of beads were also investigated. We compared the incorporation of herringbone structures to enhance mixing, and the target analyte capture both experimentally and theoretically. Notably, the measurements obtained from our theoretical model closely matched those from experiments, suggesting that this model can be employed prior to the experiments for optimizing device and assay design. Finally, using a kinetic model, we investigated if the equilibrium is achieved inside our mixing device at different flow rates.

1.7.2 Chapter 3: Detection of Toxins from Water Sample with an Integrated Microfluidic Device Coupled with Image Recognition Platform

In this chapter, we present a platform, called "Toxin-Chip", capable of rapid and parallel analyses of multiple toxins in water samples. Our system combines a microfluidic chip that integrates an optimized chaotic mixing module with the collection chambers with the optical measurement to enable highly sensitive and specific detection of MC-LR and OA toxins. We have developed a bead-based competitive assay and used QDs s as fluorescence tag. Compared to other methods, bead-based assay facilitates fluorescence signal readout while increasing the sensitivity and reducing the reaction time[51]. Moreover, using QDs s instead of organic fluorophore overcomes the low signal in monitoring small toxins present at low concentrations. Our Toxin-Chip provides a novel, rapid, scalable, and cost-effective approach to multiplex and sensitive monitoring of multiple toxins in environmental samples. More importantly, Toxin-Chip can be readily modified for rapid detection of other biological toxins.

Chapter 2

Computational and Experimental Model to Study Immunobead-Based Assays in Microfluidic Mixing Platforms

2.1 Computational Model for Immunobead-Based Assays

The analyte capture on the bead surface in a microfluidic channel involves two main phenomena: bead and analyte movements and a chemical reaction. The beads and analytes move inside the microfluidic channel, and the analytes chemically bind to the cAbs that are coated on the bead's surface. Here, we, first, analytically investigated the mechanisms of these two phenomena and then derived a 3D computational model to simulate the analyte capture in the immunobead-based assays inside microfluidic channels with different designs.

2.1.1 Modeling the Movement of Beads and Analytes

In microfluidic mixing, a reagent solution, which consists of beads conjugated with cAbs, and a sample solution containing target analytes are mixed as they flow inside a channel (Figure 2.1A, left). We studied the movement of analytes and beads by determining their

velocities in the microfluidic channel. Such information paves the way to quantify the chemical binding in the next model. A variety of factors affect the velocity profiles, such as flow rate, fluid viscosity, analyte diffusion, and channel designs. Navier-Stokes equation (2.1), which describes the fluid flow[52], can be used to determine the analyte velocity as they perfectly follow the carrier liquid streamline due to their infinitesimal size. In another word, the analytes are only under influence of the drag force.

$$\rho(V.\nabla)\overrightarrow{u} = -\nabla P + \mu \times \nabla^2 \overrightarrow{u} \tag{2.1}$$

In equation 2.1, $\overrightarrow{u}$, P, ρ, and μ define velocity, pressure, density, and kinematic viscosity, respectively. The beads, on the other hand, may experience other secondary forces that cause them to move laterally in the channel or even with a different velocity in the flow direction. These secondary forces could be exerted on the microbeads either internally for example in the inertial-based microfluidics[53, 54] or externally such as in the dielectrophoretic-based microchips[55]. Therefore, the microbeads trajectory could be controlled independently by eliminating the drag force effect in appropriate circumstances.

In nonuniform concentrations, analyte molecules diffuse and leave the fluid streamlines[56]. As a result, convection and diffusion are both responsible for analyte movement and dispersity in the microfluidic channel. Here, we have used the convectiondiffusion equation (2.2) to determine the analyte concentration profile throughout the channel in an incompressible fluid. This profile determines the quantity of analytes in the bead's vicinity, which is required to calculate the number of captured analytes on the bead's surface.

$$\frac{\partial C}{\partial t} + \overrightarrow{u}.\nabla C = D_m \times \nabla^2 C \tag{2.2}$$

In equation 2.2, C is the analyte concentration, $\overrightarrow{u}$ is the analyte velocity (which here equals flow velocity), and D_m is the analyte diffusion constant. The resulted concentration and velocity profiles of analytes provide us with enough information to study them at every given time in every location inside the microfluidic channel.

2.1.2 Modeling the Analyte Capture on Bead Surface

We implemented equation 2.3 to determine the chemical interaction between the analyte molecules and the cAbs coated on the bead surface.

$$C_0 + C_{ab} <=> C_b \tag{2.3}$$

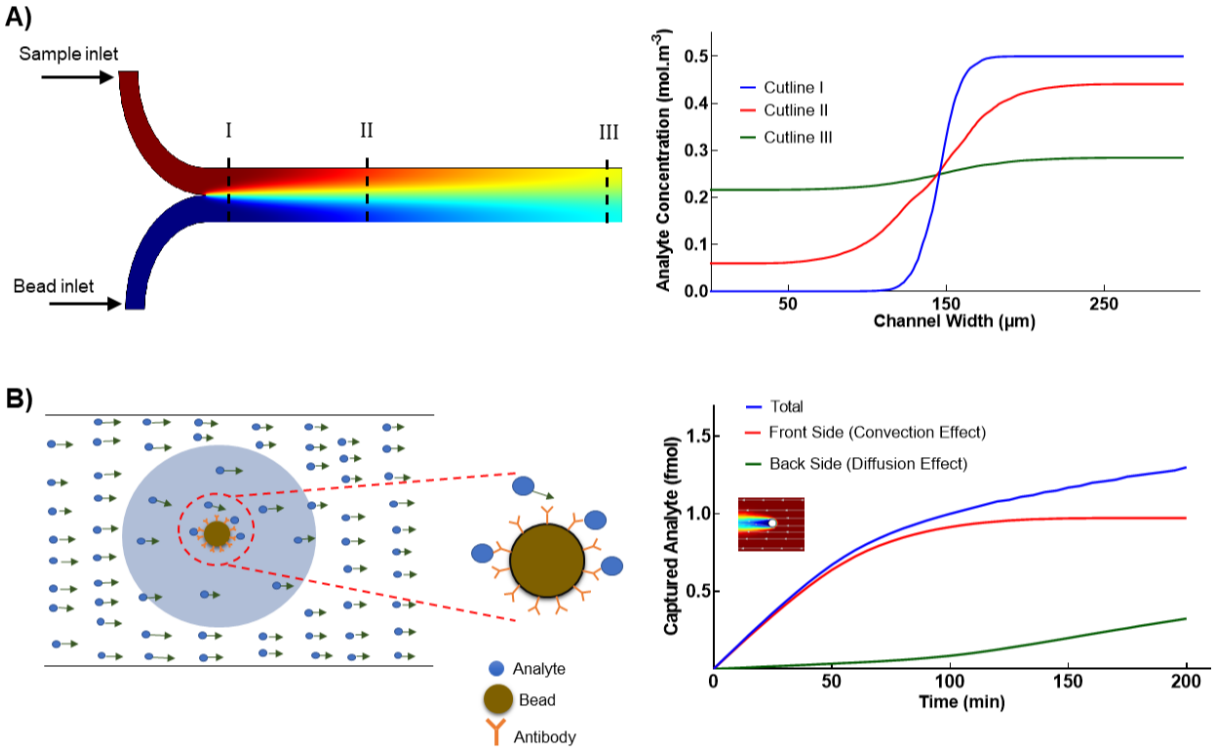

Figure 2.1: Overview of the model for simulation of the immunobead-based assay inside the mixing module. (A) Left: Simulation of two flows (sample and reagent) entering and mixing inside the microchannel. Right: Concentration of the analyte (y-axis) vs the width of the channel (x-axis) at different cutlines (I, II, III) along the microchannel. Analytes disperse in the channel and develop a uniform concentration profile. (B) Left: Schematic illustration of a bead affecting the analytes in the capture circle. Analytes enter the capture circle along their path, and some analytes are captured via the immobilized antibodies on the bead. Right: Simulation results of the captured analyte on the front and back side of the bead's surface by time. The Y-axis shows the amount of the captured analyte, and the X-axis is the time that the bead travels inside the channel.

In this equation, C_0 is the analyte concentration around the bead, C_{ab} is the available antibody concentration on the bead surface, and C_b is the concentrations of captured analytes on the bead surface. We then used the kinetic equation (2.4) to derive the rate of analyte capture.

$$\frac{\partial C_b}{\partial t} = k_{on} \times C_0 \times C_{ab} - k_{off} \times C_b \tag{2.4}$$

where k_{on} and k_{off} are the association and dissociation constants of the reaction, respectively, and show the antibody affinity toward the analyte. Higher k_{on} and lower k_{off} means higher affinity and are more favorable[57]. As explained above, C_0, can be derived from equation 2.2. C_{ab}, k_{on} and k_{off} are experimentally determined parameters. equation 2.4 can be then solved to calculate the C_b. These four equations equip us with all information we need for calculating the captured analyte concentration on the bead's surface in an arbitrary microchannel geometry in different conditions.

2.1.3 Implementing the 3D Models in COMSOL Multiphysics

We have incorporated the above two models (movement model and capture model) and implemented the four equations in COMSOL Multiphysics using Finite Element Modeling to develop a 3D model, investigating the immunobead-based assays in the microfluidic channel. This model divides the complicated channel body into small elements (the mesh). The equilibrium equations need to be satisfied over a finite number of elements instead of the entire channel. First, the movement model solves equations 2.1 and 2.2 in the channel, attaining the analyte velocity and concentration profile in the channel (Figure 2.1A). As the particle Reynolds number in our experiment and simulation conditions falls below one ($Re_p = 0.1$), we assumed that only viscous drag forces act on the beads, i.e., the finite dimensions of the channels and inertial forces are ineffectual on particle trajectory and they follow the fluid streamlines. In the movement model, analyte propagation through the channel could be considered independent of the bead presence. The beads exert influence on only a negligible portion of analytes in their proximity, which will be addressed and taken into account in the capture model. Figure 2.1A, right, shows that analytes reach a uniform profile as they travel through the channel. Next, the generated profiles were incorporated into the capture model to obtain the captured analytes on the bead surface based on equations 2.3 and 2.4.

In our model, we investigated two problems: a single bead in the channel and multiple beads in the channel. In a single bead problem, the amount of captured analytes is much less than the available analytes in the channel. We assume that as a bead moves in the channel, only analytes inside a finite region and at the bead's vicinity are captured. We called this region as the capture circle. In our model, the capture circle is defined as the boundary where, beyond that, the analyte concentration is not affected by the presence

of the bead. In addition, we assumed that the analyte concentration on the boundary of the capture circle is constant and uniform for the sake of simplicity. This assumption is valid because the uniform analyte condition could be attained within only 12 cm (Figure 2.1A, after cutline III) from the inlet, while the channel length in our simulation and experiment is 35 cm. The capture model consists of two concentric circles, the smaller one representing the bead and the bigger circle representing the capture circle (Figure 2.1B, left). The analytes move inside the capture circle with the flow regime derived from the movement model and are depleted as they are captured on the antibody-conjugated bead. However, the analytes outside of the capture circle restore the consumed analytes. This effect has been modeled by considering a constant concentration over time at the perimeter of the capture circle. The concentration gradient of the analyte inside the capture circle is calculated by solving the convection diffusion equation (equation 2.2). The boundary conditions are the indefinite analyte supplement from capture circle boundary (equation 2.5) and the capture of analytes on the bead's surface (equation2.6). Initial conditions are also given in equation 2.7 to solve time-domain equations.

$$C = C_0 \quad at\ R_c\ ,\ t \geq 0 \tag{2.5}$$

$$\begin{cases} N_A D_m \frac{\partial C}{\partial r} = k_{on} \times C \times (C_{ab} - C_b) - k_{off} \times C_b \\ \frac{\partial C_b}{\partial t} = k_{on} \times C \times (C_{ab} - C_b) - k_{off} \times C_b \end{cases} \quad at\ R_b \tag{2.6}$$

$$C = C_0\ ,\ C_b = 0 \quad at\ t = 0 \tag{2.7}$$

In these equations, r, C, D_m, R_c, k_{on}, k_{off}, C_b, R_b, and C_{ab} are the distance from the bead center, the analyte concentration, the analyte diffusion constant, the capture circle radius, the association constant, the dissociation constant, the concentration of captured analytes on the bead surface, the bead radius, and the initial antibody concentration on the bead surface. In a more practical scenario with multiple beads, the presence of beads cannot be neglected. This problem requires the development of a time-changing concentration profile based on the total captured analytes on the beads.

This study reports the concentration of captured analytes over time on the bead surface in the microfluidic channel. At the outset, there are many antibodies available on the bead surface and the analytes are captured at a constant rate; however, the antibodies on the bead's surface get occupied, resulting in a drop in the capture rate until the bead becomes totally saturated. This effect is simulated using our model and shown in Figure 2.1B, right, where the total captured analyte concentration is shown in blue. Interestingly, the total

captured analyte does not reach the saturation state. This is a result of bead movement that causes the front side of the bead to encounter fresh analytes, while the back side is left with not enough available analytes to recombine and the capture rate on this side is very slow (Figure 2.1B, right-inset). The captured analyte on the front side saturates rapidly and accordingly; we can conclude that capture mostly occurs on the front side of the bead. In real conditions, beads rotate in a microfluidic channel and the captured analytes are distributed on the bead's surface. This rotation is because of the variation of shear rate distribution throughout the channel width. In the case of Newtonian fluids and for a laminar flow where the layers of the fluid move in parallel with different velocities, a particle rotates with a speed of ω (rad/s) equal to half the vorticity, which could be calculated using the below equation.

$$\omega = \frac{\dot{\gamma}}{2} \tag{2.8}$$

In equation 2.8, $\dot{\gamma}$ is the average shear rate across the particle. Therefore, rotation of the beads must be considered in the modeling to find the exact saturation time, but this also impedes the model simplicity. A solution to circumvent this issue is to use the capture rate as the measure of capture performance instead of saturation time since the total capture rate is equal to the capture rate on the front side at the beginning of the reaction.

2.2 Results and Discussion

2.2.1 Studying the Effect of Bead Movement

The microfluidic channel designed for the simulation experiments has a width of 300 μm, a height of 45 μm, and a length of 35 cm. In our model and experiments, the capture of IgG (as an analyte) was investigated using IgG cAbs-coated beads. Table 2.1 summarizes the parameter used in this paper.

In the first step, we calculated the diameter of the capture circle based on the bead diameter (d). A smaller capture circle contains less amount of analytes. Thus, the dimension of the capture circle can affect the modeling results and a critical minimum diameter should be considered to have comparable results. To obtain this critical diameter, we considered a scenario where the convection is zero and the capture happens via the slow diffusion transport. The diameter of the capture circle derived in this situation can be

Table 2.1: Parameters used in the simulation

parameters	**unit**	**value**
flow rate	μL/min	15
channel height	μm	45
channel width	μm	300
channel length	cm	35
analyte concentration	μg/mL	1
analyte diffusion constant	30 cm$^2/s$	2.8×10^{-7}
analyte molar mass	g/mol	15×10^4
association constant[57]	1/M·s	3.3×10^4
dissociation constant[57]	1/s	2.9×10^{-4}
antibody surface density[20]	mol/m^2	8×10^{-6}
antibody molar mass	g/mol	15×10^4

then applied in other situations where the restoration of the analytes in the capture circle happens faster due to convection. In a single bead problem, for a bead diameter of 4.5 μm, we investigated the analyte capture using different capture circle diameters (R_c = 2d to 14d) to define the critical diameter. As Figure 2.2A shows that, after a certain diameter (10d), the capture rate and surface concentration of the analytes do not change significantly by increasing the R_c. We considered the 10d as the R_c in the next studies. Figure 2.2A reports results in terms of the capture rate and total captured analytes. The capture rate indicates the speed of the binding process, and the captured analyte reports the amount of analytes that are captured on the bead at the end of the microfluidic channel. We have calculated R_c for beads with different diameters (1–8 μm) in a simple channel and observed that R_c is independent of d (Figure A.1). To have a universal R_c for all bead diameters, we have chosen 10d. We acknowledge that other sizes could have been chosen as the R_c but decide to keep a safety margin so that in the more complex channel geometries (such as herringbone structures) no issues are encountered.

In practical situations, nonspecific bindings interfere with the target analyte capture. We have simulated the effect of nonspecific bindings by considering three parallel reactions with different k_{on} and k_{off} on the bead's surface (Tables A.1). The simulation results (Figure 2.2B) show that the existence of nonspecific bindings decreases the capture efficiency of the target analyte. Beads could be manipulated using external forces in a channel and have a lateral movement in addition to their primary trajectory. Here, we simulated the sinusoidal movement of a bead in a simple microchannel (Figure 2.3A-C). The bead moves in a channel occupied with analytes, and the frequency and amplitude of its movement in-

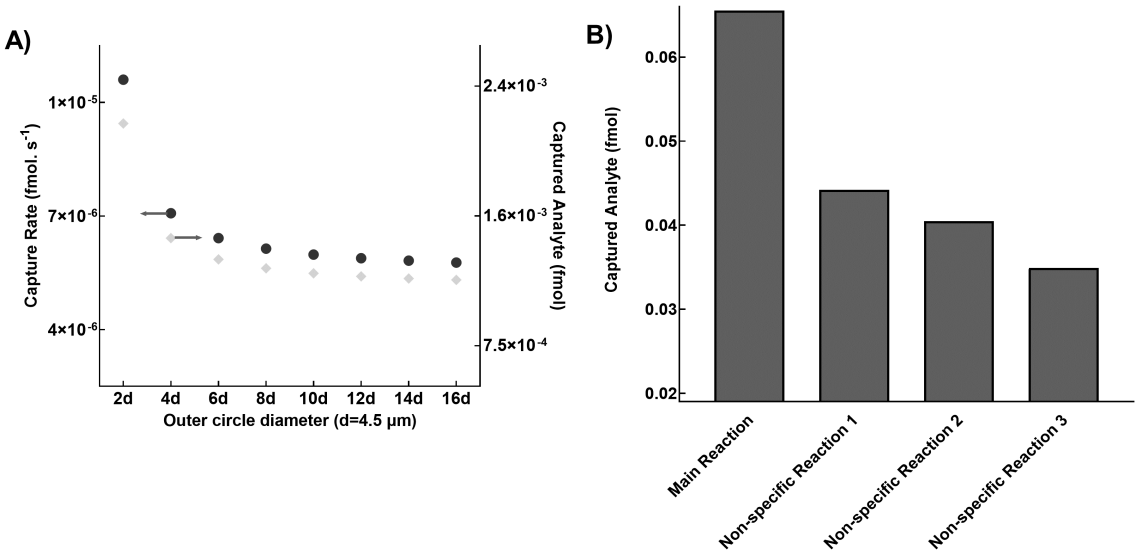

Figure 2.2: (A) Optimization of the capture circle diameter based on the bead diameter. (B) Effect of nonspecific binding on the capture of the target analyte. Each column shows the amount of the captured target analyte in the presence of a particular nonspecific reaction. This figure reports simulation results.

dicate the position and velocity of the bead by time. The bead movement was studied in a relative velocity of analytes to the bead and the model was trained based on the sinusoidal movement of the bead. Figure 2.3D shows the concentration profile around the bead. An alternating pattern was observed in the analyte profile, which indicates the effect of the sinusoidal trajectory of the bead. The analyte-free zone (blue tail of bead) shows the trace of the bead movement in each phase of its trajectory ($\phi = 0$, $\pi/2$, and π).

We first investigated the effect of change in the amplitude of bead trajectories (Figure 2.3A). We observed that by increasing the domain of bead movement, a higher capture rate is achieved. This is due to higher bead lateral velocity, which increases the relative analyte velocity toward the bead. Figure 2.3B investigates the increase in the frequency of the bead movement. A higher frequency results in higher fluctuations in the bead movement and more analytes enter the capture circle, enhancing the binding opportunities in the capture zone. A considerable change in the level of captured analytes caused by different bead moving patterns (Figure 2.3A,B) was observed. It confirms that the bead lateral movement vividly affects the analyte capture in the immunobead-based assays in microfluidic devices and introducing a secondary force can improve the capture[58, 59].

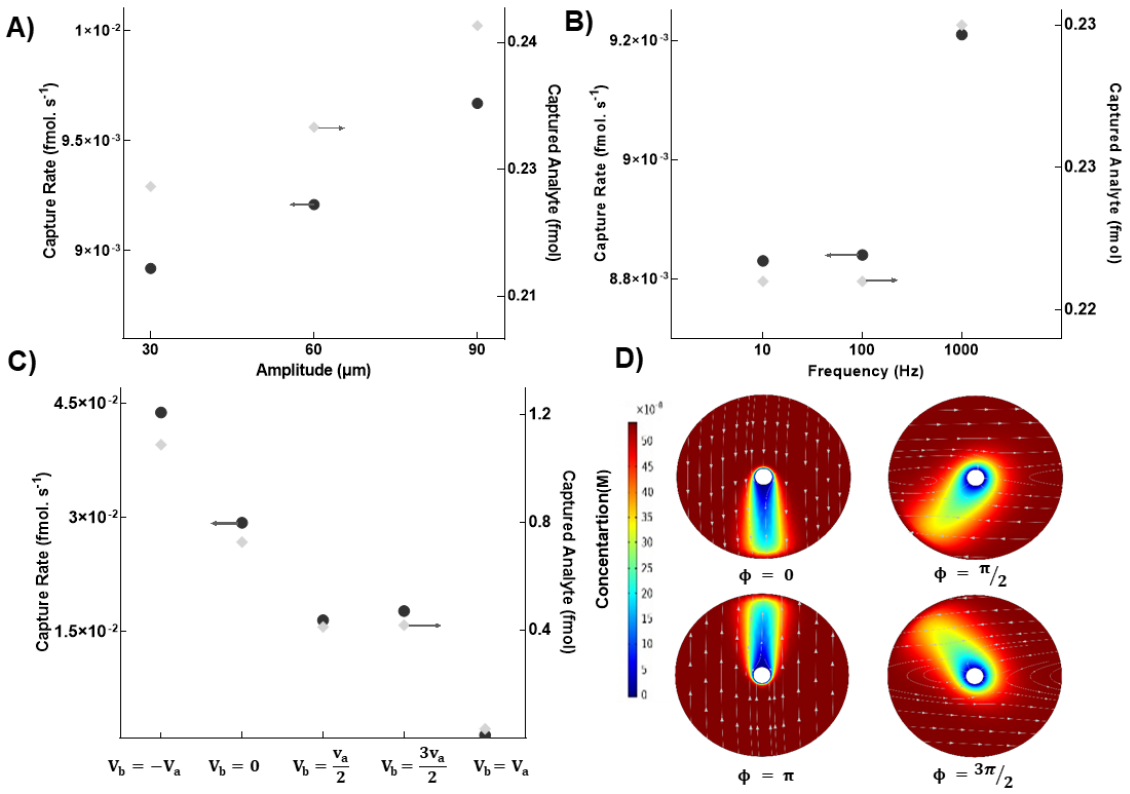

Figure 2.3: Amplitude (A) and frequency (B) of the bead's sinusoidal trajectory on the captured analyte on the bead. (C) Effect of the bead and analyte movement pattern (the relative velocity of the bead and analyte) on the captured analyte. V_b and V_a denote bead and analyte velocity, respectively. (D) Cross section of analyte concentration inside the capture circle during bead's sinusoidal movement. The magnitude and direction of relative velocity oscillate, which in turn shape the analyte concentration profile. This figure reports simulation results.

Immunobead-based assays have been optimized by employing new channel designs or applying an external force (magnetic or dielectrophoretic forces) to manipulate the bead movements[60]. Our model is capable of simulating various movement patterns in the microfluidic channel. In Figure 2.3C, different strategies that a bead and analytes encounter were studied: (1) the bead and analytes move with the same velocity but in the opposite directions ($V_{analyte} = V_{bead}$); (2) the bead is immobilized and analytes move ($V_{bead} = 0$; (3) they move in the same direction but analytes move faster ($V_{analyte} > V_{bead}$), (4) bead velocity is higher ($V_{analyte} < V_{bead}$); and finally (5) the bead and analytes move with the

same velocity and direction ($V_{analyte} = V_{bead}$). The reported results signify the effect of convection on the immunobead-based assays. In condition#1, the highest relative velocity and the maximum capture efficiency are achieved. On the contrary, the relative velocity in condition#5 is zero and the lowest amount of analytes gets captured. Condition#3 and #4 confirm the role of relative velocity, although the bead velocity changes but the relative velocity is the same. Thus, the capture rate and captured analytes are the same among these two conditions.

2.2.2 Studying the Effect of Bead Diameter and Number

Next, we investigated the influence of changes in the bead diameter and number on the assay performance in the microfluidic channel. It was assumed that, in a multiple bead problem, every bead has its own capture circle with no interference from other beads. However, the diameter of the capture circle and the analyte restoration process are affected by the bead number and diameter. In our 3D model, the restoration process happens via the analytes present on the boundary of the capture circle. In the single bead problem, there is an excess of unbound analytes, and hence, the concentration on this boundary is constant. However, in the presence of other beads, the analytes are captured all over the channel, and the input concentration to the capture circle decreases over time. In the multiple bead problem, the volume of the microfluidic channel (V_c) is divided between the beads to calculate the R_c. If N is the number of beads present in the channel at any given time, R_c is given by equation 2.9.

$$V_c = \sqrt[3]{\frac{3V_c}{4\pi N}} \tag{2.9}$$

The analytes were assumed to be uniformly distributed in the channel, and the same share of analytes was allocated to each bead. This model is different from the single bead problem where all of the analytes in the channel were determined as a single bead's share. To solve the multiple bead problem, the captured analytes were then subtracted from the bead's share of analytes in every time step, achieving a time-changing concentration for the available analytes on the boundary of the capture circle.

Figure 2.4 reports the number of analytes captured by different bead sizes with the same surface area (a higher number of beads for smaller bead size) (Figure 2.4A,C) and different bead numbers (Figure 2.4B,D). To simplify the model, the beads were assumed to move in the center of the channel one by one. We considered a constant cAbs density on the bead's surface; hence, a larger bead has more available capture sites and captures more analytes,

confirming our simulation results in Figure 2.4A (black circles). The captured analytes per bead grow quadratically as the number of antibodies on the bead is proportional to the square of bead diameter. The fixed total surface area and cAbs density lead to a constant total number of antibodies on beads with different diameters. We observed that total captured analytes (represented by the gray square) decrease by increasing the bead diameter. As the bead size increases, more cAbs are available per bead and the analytes in the vicinity of the beads are consumed faster and fresh analytes should be resupplied from remote regions. Therefore, by increasing the bead diameter and in conditions that a reaction is constrained by a transport mechanism (i.e., in the straight channels where diffusion is the dominant method), the total captured analytes are affected by a slower supply of uncaptured analytes. The Damkohler number (D_a), which defines the ratio of the reaction rate to the transport mechanism, explains this observation. The D_a for the convective mass transport mechanism (equation 2.10) reports a constant number for all bead sizes, suggesting that the bead diameter does not affect the convection mechanism. However, in the D_a equation for the diffusion mass transport mechanism (equation 2.11), D_a increases by increasing the bead diameter (d). The larger D_a shows that the situation is diffusion-limited, i.e., it takes longer for the analytes to reach the surface of the bead and react with the antibodies, which confirms our simulation prediction.

$$D_a = C_b \times k_{on} \times t_{residual} \tag{2.10}$$

$$D_a = \frac{C_b \times k_{on} \times d}{D_m} \tag{2.11}$$

Figure 2.4B presents the results of using different numbers of beads (for d = 4.5 μm). At low bead numbers, enough analytes are available for each bead and the target capture occurs in the antibody-limited regime. At the low bead number, by increasing the bead numbers, the captured analytes per bead decrease, while the total number of captured analytes increases. As the number of beads increases, we expect that (1) the capture circle becomes smaller and the number of available analytes for each bead decreases and (2) the capture regime is changed from antibody-limited to analyte-limited. As a result, the number of analytes per bead decreases (black circles) and the number of total captured molecules starts to saturate (not shown in the simulation).

We fabricated a microchannel using a standard microfluidic device fabrication protocol with glass substrates and poly-dimethylsiloxane (PDMS) and performed immunobead-based sandwich ELISA experiments to validate the modeling results. For this purpose, a microchannel with a total length of 35 cm and a cross section of 300 μm $\times$ 45 μm

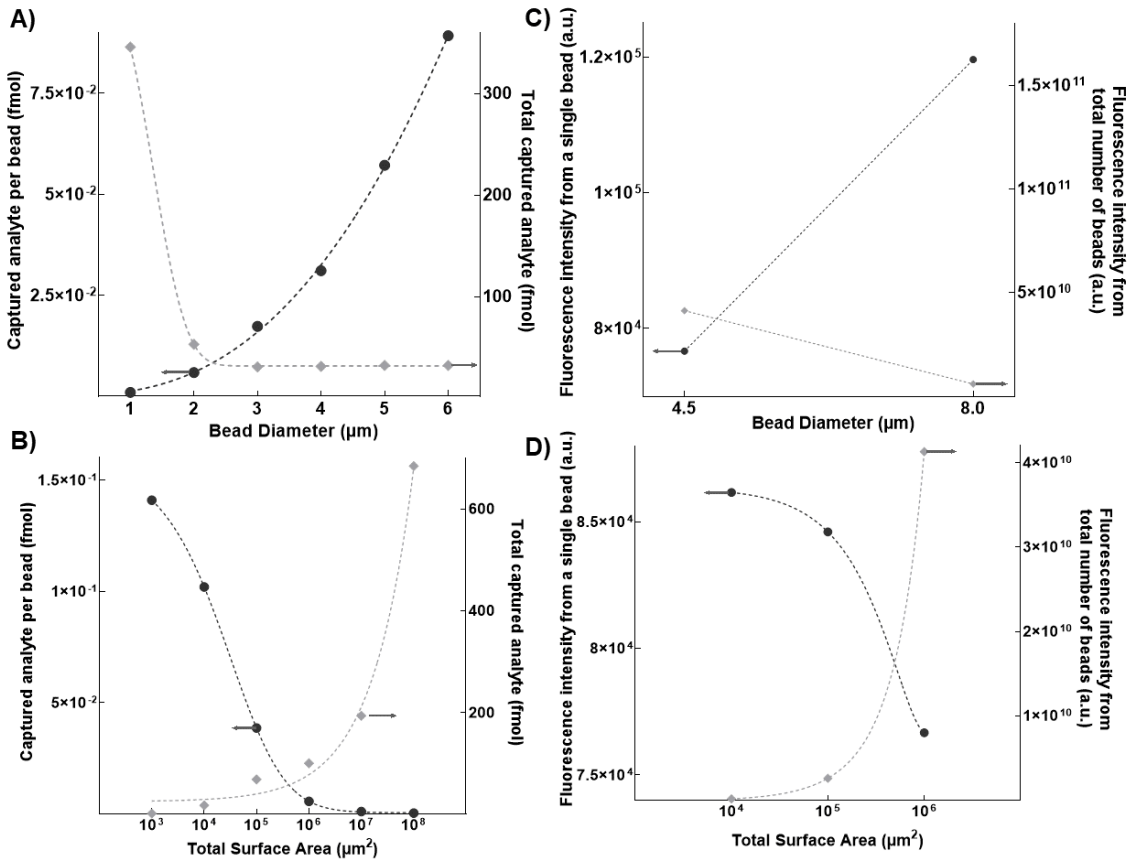

Figure 2.4: Simulation and experimental results of the immunobead-based assay in multiple bead situations using different diameters and numbers. (A) Captured analytes vs bead diameter for multiple beads with a fixed total area. Here, the number of beads in the channel decreases as the bead's diameter increases. (B) Change in the amount of captured analytes vs different bead numbers with the same bead diameter. Here, the number of beads increases as the total surface area of beads increases. Experimental results of immunobead-based sandwich ELISA for IgG capture performed with (C) different sizes (4.5 and 8 μm) and different numbers of the bead (bead size: 4.5 μm) in a microchannel (D).

was designed in a serpentine shape to fit dimensions of regular glass slides (the radius of the turns in the serpentine shape is large so the effects of these turns can be neglected). Immunobead-based sandwich ELISA was performed to capture IgG with a concentration of 1 μg/mL. The reagent solution consisting of microbeads functionalized with IgG cAbs and fluorescently tagged dAbs (10 μg/mL) was introduced through the reagent inlet, while

a buffer solution containing IgG was injected via the sample inlet. We injected these solutions at a flow rate of 15 μL/min and then collected the beads from the device outlet and measured the fluorescence signal using flow cytometry. Two sizes of beads (4.5 and 8 μm) were chosen to investigate the effect of bead diameter on the analyte capture inside the channel. Figure 2.4C reports the same trend observed in the simulation results (Figure 2.4A). A higher number of cAbs are immobilized on the 8 μm bead compared to the 4.5 μm one, resulting in the capture of more analytes and thus increased fluorescence signal. However, the fluorescence signal collected from the total number of beads is less, as predicted by the modeling results. The effect of the number of beads has also been experimentally investigated. Three different bead numbers were injected into the device, and the fluorescent signals collected from one bead or the total number of beads were measured (Figure 2.4D), confirming the simulation results reported in Figure 2.4B.

We have also studied the effect of the bead diameter on the total/front side/back side captured analyte rate for a single bead, assuming a constant amount of capture antibodies (Figure A.2). In a larger bead, capture antibody molecules are dispersed over a larger area, resulting in a greater number of analytes per capture antibody molecule. Therefore, the capture rate increases by increasing the bead diameter while the amount of capture antibodies is constant. In immunobead-based assays, the steric hindrance effect is an unanticipated issue. To study if our model can account for the steric hindrance effect, we have calculated the capture rate over time for different antibody concentrations on the bead's surface. We observed that as the antibody concentration increases, the bead captures more analytes (Figure A.3). Due to the limited number of analytes in the channel, an increment in antibody concentration after a certain point does not change the trendline. These results show that our finite element method model cannot account for steric hindrance.

2.2.3 Chaotic Flow Mixing vs Laminar Flow Mixing

Here, we have studied the effect of channel geometry on the analyte capture. As was discussed, the number of analytes captured on the beads is relatively proportional to the number of adjacent analytes and antibody binding sites. In a chaotic flow, the analytes move randomly, creating a higher capture chance. The laminar flow regime in the microfluidic channels hinders the efficient binding on the bead because the mixing is minimized. Various groups have presented innovative designs to induce chaos in the laminar flow regime of microfluidic channels for enhancing the analyte capture rate. These designs are called micromixers and can be categorized into two groups of active and passive mixers[19]. Generally, active mixers use an external force to disturb the fluid flow[61, 62, 63], while the passive mixers implement alteration in the channel path including turns and obstacles to

induce agitation[64, 65, 66]. A prominent geometry used in this regard is called herringbone structures that consist of repeated patterns on top of a channel (Figure 2.5A).

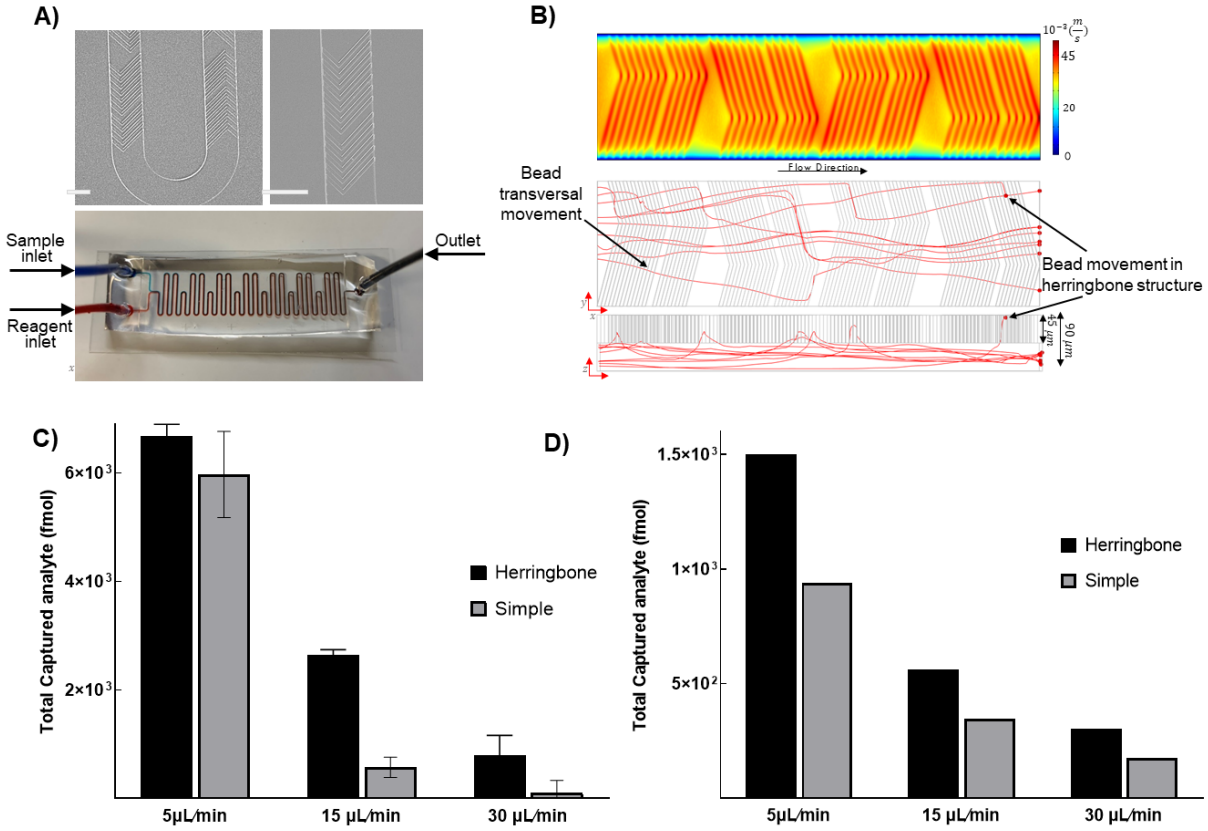

Figure 2.5: (A) Fabricated herringbone-structured serpentine channel, top: microscopic images from the channel. The grooves are the herringbone layer of the channel, bottom: two fluid flows (represented with two different colors) mix inside the channel. (B) Herringbone channel simulation, top: velocity profile inside the herringbone channel, bottom: simulated bead's trajectory inside the channel. The effect of the agitated flow pattern (effect of herringbone structure) on the beads' movement pattern is clear. (C) Experimental and (D) simulation results of comparing the amount of IgG captured on the bead in simple and herringbone-structured channels in different velocities.

We have employed our 3D model and investigated the capture of analytes using both simple and herringbone microchannels. Additionally, we have fabricated microchannels with herringbone structures and compared the simulation and experimental results. Herringbone structures induce perturbations and transversal movements, which result in nonuni-

form velocity profiles[67, 68] (Figure 2.5B, top). The bead trajectory governed by the new velocity profile inside the herringbone structures was also simulated (Figure 2.5B, bottom). To achieve a chaotic flow, herringbone structures with a height of 45 μm were added to the top of the simple channel. Both devices had two inlets for sample and reagent injection and one outlet where the beads were collected (Figure 2.5A). In this model, the direction of the applied drag force constantly changes, and beads change their movement direction in all three dimensions and even enter the herringbone structures, leading to increased residual time and a greater chance of collision with fresh analyte molecules.

The immunobead-based sandwich ELISA was performed in both simple and herringbone-structured microfluidic devices to capture IgG with a concentration of 1 μg/mL. A reagent sample consisting of microbeads (d = 4.5 μm) functionalized with IgG cAbs (10^5 bead/mL) and fluorescently tagged dAbs (10 μg/mL) were introduced through the reagent inlet, while a buffer solution containing IgG was injected via the sample inlet. We injected these solutions at different flow rates (5, 15, 30 μL/min) and then collected the beads from the module outlet and measured the fluorescence signal using flow cytometry (Figure 2.5C). After this measurement, we have used the IgG bead-based ELISA calibration curve (shown in Figure A.4) to correlate the measured fluorescence signal to the amount of the captured analyte on the bead. Comparing the amount of the captured analyte at different flow rates using simple and herringbone channels showed that herringbone structure is more effective to capture IgG. Herringbone structure enhances the rate of molecular diffusion and reduces the required incubation time. Specifically, at the flow rate of 15 μL/min, capture efficiency is significantly enhanced compared to other flow rates. This is because of the trade-off between the bead's residual time and agitation inside the channel. At lower flow rates, residual time increases but the agitation is unlikely to happen, whereas at higher flow rates, the flow is more agitated, and beads spend less time in the channel. We simulated the target capture using our 3D model in simple and herringbone structures (Figure 2.5D). The simulated results correlated well with the experimental results and attested the effect of incorporating herringbone structures to improve capture efficiency at each flow rate.

2.2.4 Kinetic Model of the Herringbone Channel

In the final step, we modeled the kinetics in the herringbone device to investigate if the equilibrium is achieved inside the device[20] for different flow rates of 5, 15, and 30 μL/min. The mixing time inside the device depends on the diffusivity constant (D) and the length over which diffusion must act to homogenize the concentration, known as the striation length (st). The mixing time is then given by

$$t_{mixing} = \frac{st^2}{D} \tag{2.12}$$

In chaotic microfluidic mixing, Baker's transformation illustrates that st can exponentially decrease, and at the optimum flow velocity, this is shown by[69]

$$st = st_0 \times 2^{-n} \tag{2.13}$$

where n is the number of chaotic advection structures (here, the number of grooves in each cycle = 5). Therefore, in our herringbone mixing system, the time of mixing can be calculated as

$$t_{mixing-chaotic} \frac{st_0^2 \times 2^{-10}}{D} = \frac{st_0^2}{D \times 2^{-10}} = \frac{st_0^2}{D_{eff}} \tag{2.14}$$

Hence, in the chaotic mixing scenario, diffusion can be increased approximately 1000-fold. On the other hand, the Smoluchowski result has shown that the k_{on} can be approximated as linearly proportional to the diffusion constant. Thus, chaotic mixing within the herringbone device could potentially increase the value of k_{on} by 1000-fold. However, k_{on} cannot increase beyond 10^6 1/M·s due to the orientational constraints of the biomolecular interaction[70]. Thus, when modeling the kinetics in the herringbone device, we assume that k_{on} equals this upper bound of 10^6 1/M·s.

In the herringbone device, the values of k_{on},k_{off}, and K_D are then as follows: $k_{on} = 10^6$ 1/M·s (upper bound from orientational constraints), $k_{off} = 2.9 \times 10^4$ 1/s (k_{off} of a monoclonal Ab)[57], and $K_D = 3.45 \times 10^9$ M (obtained by the ratio of k_{off}/k_{on}). A model to investigate quantitatively whether equilibrium is achieved inside the herringbone device was developed using these estimated values of K_D, k_{on}, and k_{off} of the IgG cAbs. The fluorescence signal intensity is related to the IgG concentration (C), k_{off}, k_{on}, and time based on the below equations

$$I_t - I_{bg} = I_{max} \times (1 - exp(-k_{on}Ct - k_{off}t)) \tag{2.15}$$

$$I_{max} = \frac{A \times [IgG]}{[IgG] + K_D} \tag{2.16}$$

where I_{bg} is the background signal and A is an experimentally determined proportionality constant. We plotted equation 2.15 as a function of time for different IgG concentrations

(Figure 2.6A) and observed that reaching equilibrium within the mixing module would take 10–30 min. Given that the incubation time in the herringbone device for flow rates of 5, 15, and 30 μL/ min is 60, 20, and 10 s, we can conclude that equilibrium is not reached within our device.

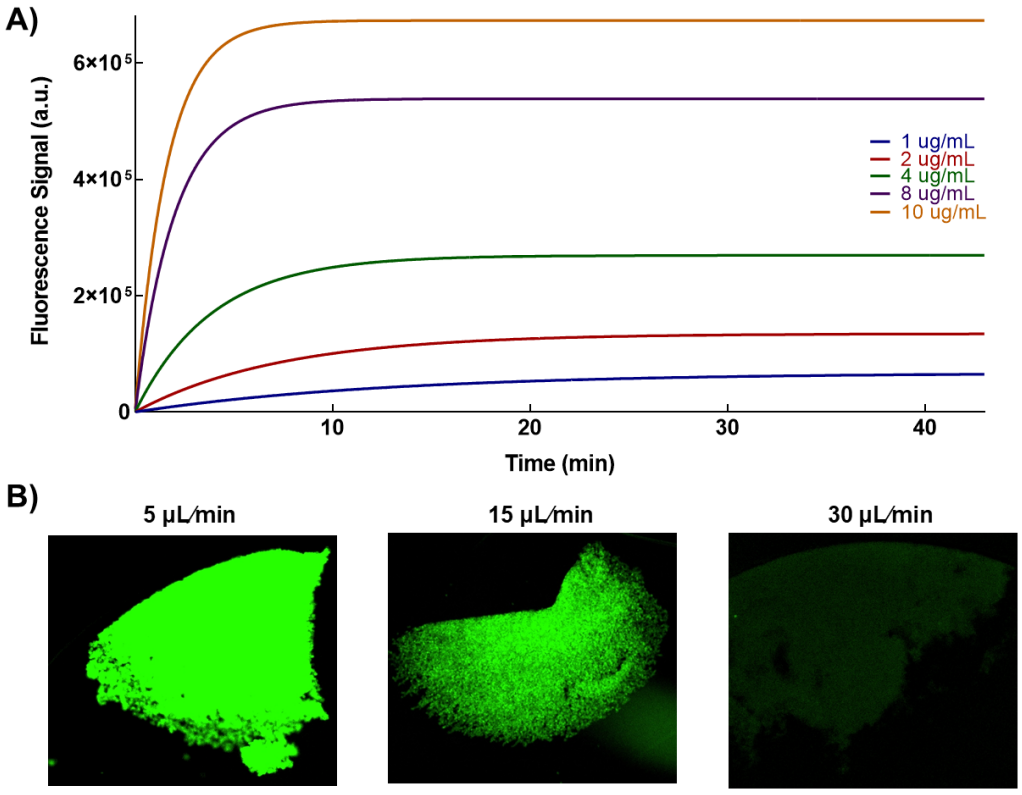

Figure 2.6: (A) Modeling of fluorescence signal intensity vs time at different IgG concentrations. The fluorescence signal saturation curve was calculated using equation 2.15. The parameters of the equation are attained from the experiment. (B) Microscopic images of the analyte-bound beads retained inside the detection chamber by an external magnet. The images confirm the saturation curve predictions; the fluorescence signal decreases as residual time decrease (the flow rate increases).

Figure 2.6B shows the fluorescence images of the beads collected from the herringbone device at different flow rates. As confirmed by Figure 2.6A, by increasing the flow rate, the incubation time decreases and thus the fluorescence signal decreases. The fluorescence images have been taken from retained magnetic beads in a chamber by a magnet. The

measured mean fluorescence signal from these images is 1145, 435, 100 a.u. for the flow rates of 5, 15, and 30 μL/min, respectively.

Chapter 3

Detection of Toxins from Water Sample with an Integrated Microfluidic Device Coupled with Image Recognition Platform

3.1 Detection Strategy

Bead-based, indirect competitive ELISA (Figure 3.1)was used as our toxin detection strategy. The reactive solution contains the toxin mcAb, the target toxin, and magnetic beads functionalized with the toxin, and the competition happens between the free, target toxin in the solution and bead-bound toxin molecules. In the next step, the secondary antibodies are added to the solution and serve as reporter probes. The polyclonal antibody (pAb), conjugated to QDs, is the secondary antibody that can bind to the mcAb captured on the bead surface and establish the indirect ELISA. Our toxin detection strategy is a signal-off assay. The more toxins in the sample, the more free toxins occupy the mcAb, thus less mcAb are available to bind to the bead-bound toxins. This leads to less mcAb binding to the bead surface for detection by pAb-QDs, causing a lower fluorescence signal.

In this assay, the magnetic beads are functionalized with the toxin-bovine serum albumin (BSA) compound. BSA is a carrier protein that aids in the functionalization of toxins on the surface of beads and facilitates the toxin participation in the immunoreaction without interfering with it. As a first suit of experiments, we studied different concentrations of mcAb to determine the optimal concentration for the competitive assay (Figure 3.1B).

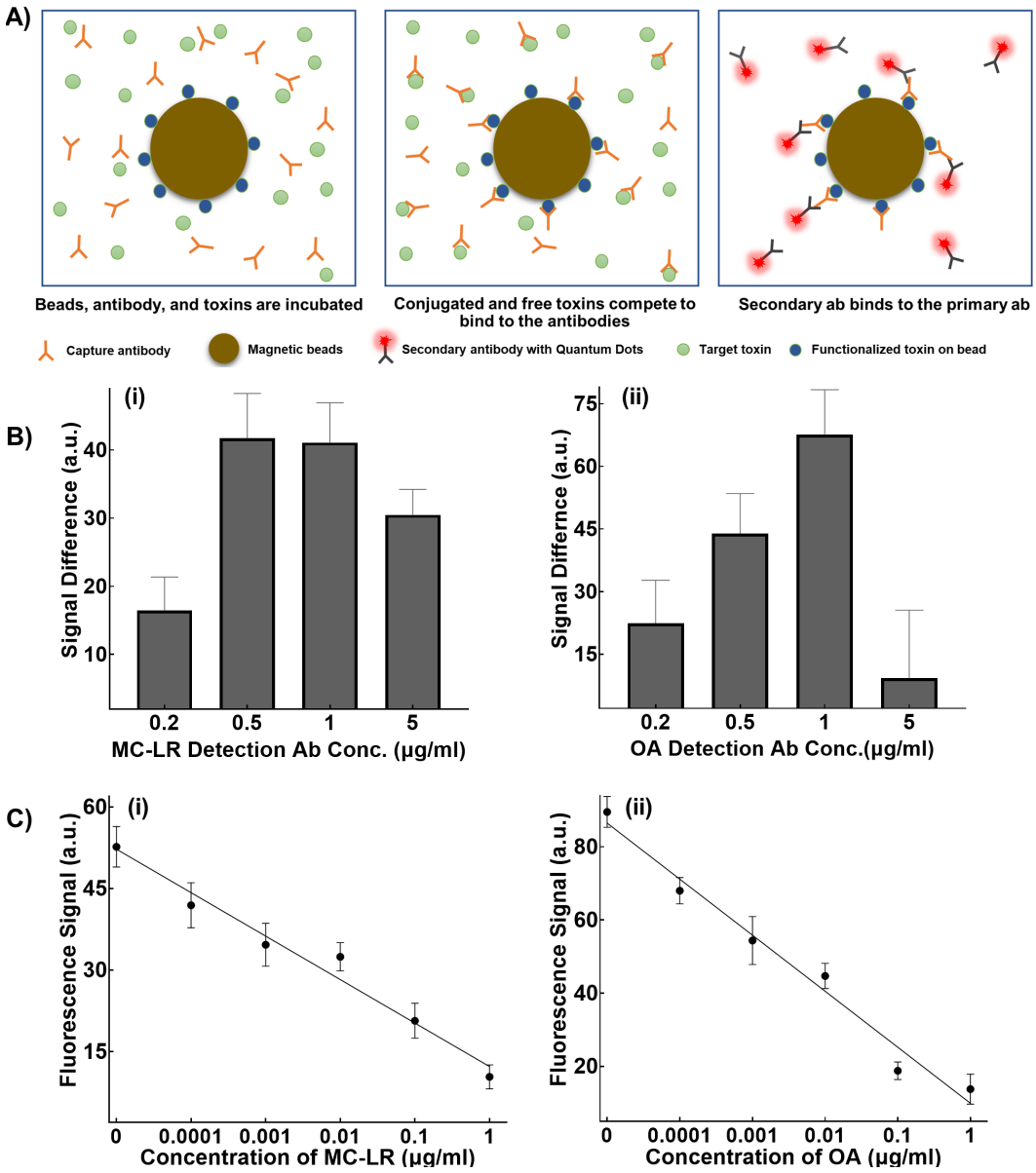

Figure 3.1: Bead-based indirect competitive ELISA assay for detection of target toxins. (A) Schematic of the assay. Microbeads functionalized with the toxins mcAb and target toxin are mixed (right), competition in the presence of toxin mcAb (center), and the pAb-QDs attached to the antibody on the surface of beads (right). (B) Investigation of fluorescence signal range between the lowest (0 g/ml) and the highest (1 g/ml) concentration of MC-LR (i) and OA (ii) at different detection mcAb concentrations. (C) The benchtop assay calibration curve. The measured fluorescence signal at each concentration of MC-LR (i) and OA (ii) is shown.

Low concentrations of mcAb result in an indistinguishable signal at the higher concentrations of toxin due to a lack of mcAb for the targets in the solution. On the other hand, high mcAb concentrations cause saturation at the lower concentrations of the target toxin as the abundance of mcAb provides sufficient antibodies to bind to the bead-bound toxin regardless of the target toxin concentration. Therefore, we tested the assay with different concentrations of the mcAb and measured the fluorescence signal difference between the highest and lowest concentration of the target toxin.

Figure 3.1B-i presents the results of MC-LR mcAb optimization and reports the 0.5 and 1 μg/ml as optimal concentrations of MC-LR indirect competitive assay. We experimented with both concentrations, and the assay performed better at 1 μg/ml, which has been chosen as the MC-LR mcAb's optimum concentration. Figure 3.1B-ii indicates 1 μg/ml as the optimum concentration of OA mcAb. With this condition, however, saturation was seen at the low end of the calibration curve. Therefore, the next candidate (0.5 μg/ml) was used as the optimum concentration and produced the calibration curve.

We initially validated the performance of our indirect competitive assay with a benchtop experiment with optimized antibody concentration (see Methods). The detection performance of this assay was verified by analyzing the different concentrations of two target toxins (MC-LR and OA) in the wide range of 0-1 μg/ml. The fluorescence images (Figure A.5) and measured fluorescence signals (Figure 3.1C-i and ii) showed a decrease in the intensity of the fluorescence signal of the beads incubated with a higher concentration of the toxin.

3.2 Toxin-Chip Fabrication and Optimization

The Toxin-Chip integrates the bead-based, indirect competitive ELISA into a specially designed microfluidic device to achieve detection of toxins. The platform (Figure 3.2) has three inlets for the injection of water sample and reagent solutions. The water sample is injected into the device through an inlet sample and is divided into two streams, and each stream is directed to its own sensing modules for MC-LR or OA detection. The sensing modules include a serpentine mixing microfluidic device for mixing target analytes with their reagent solution and a detection chamber where beads were collected for fluorescence labelling and measurement. The fluorescence images were taken from the detection chamber and processed to determine the fluorescence signal intensity and toxin concentrations.

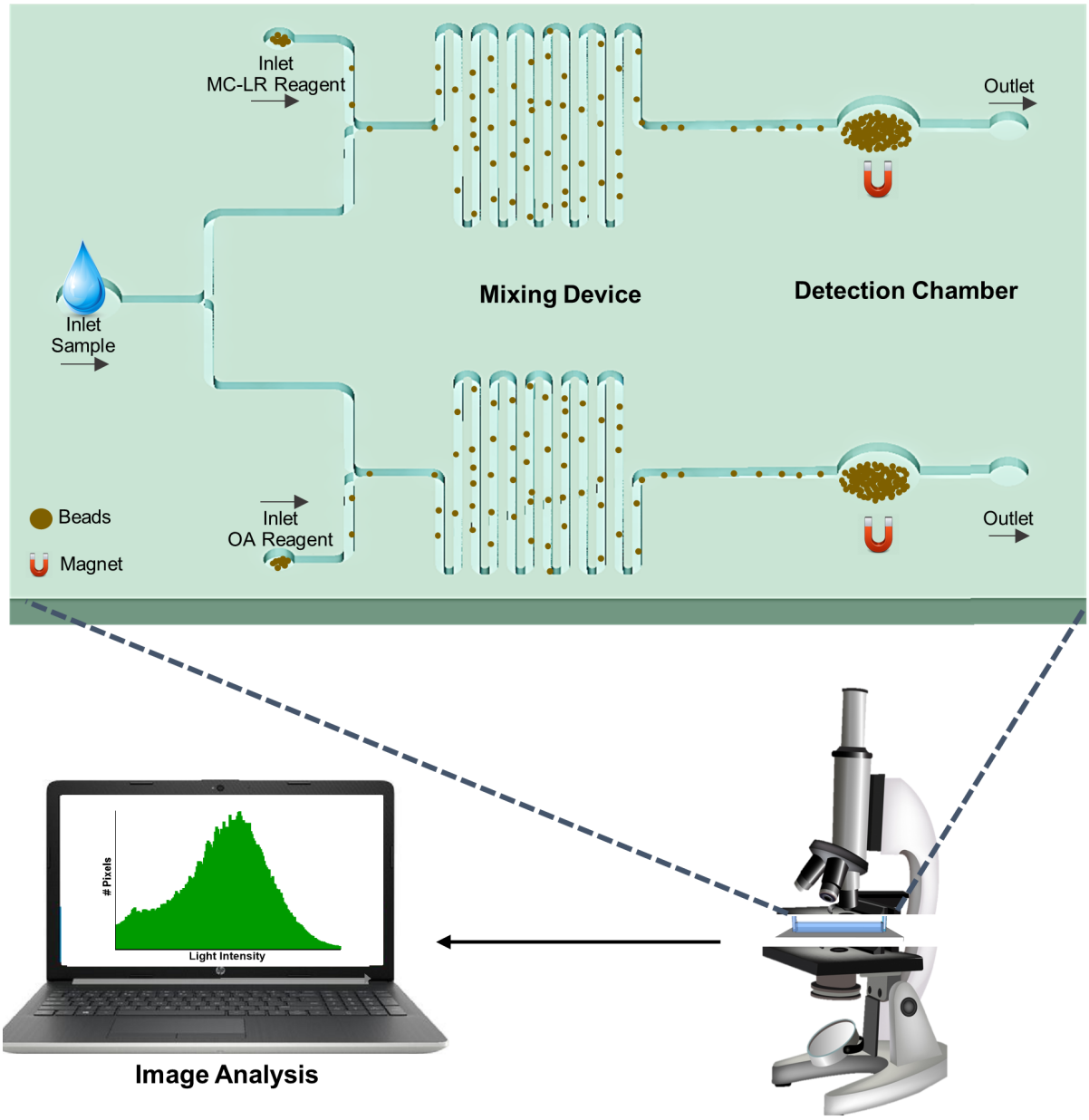

Figure 3.2: Overview of the Toxin-Chip. The water sample and reagent solutions are injected into the device using a syringe pump. The device consists of two sensing modules, each including a mixing microfluidic device where the sample is mixed with the reagent solution and a detection chamber that collects the beads for microscopic image capturing. The chamber(s) is observed under the microscope, and the images are analyzed with an image analysis program.

3.2.1 Fabrication and Optimization of the Mixing Module

Prior to the fabrication of the Toxin-Chip platform, each component of the device was individually fabricated and optimized. We have fabricated these PDMS devices using the same standard protocol (see Chapter 2).

IIn the mixing microfluidic device, the water sample and reagent solutions were injected through two inlets and efficiently mixed. The benchtop assay of toxin detection takes hours to complete, because of limited diffusion, manual pipetting, and several washing steps. The incorporation of herringbone structures into the channel design induces chaotic mixing [67] and significantly increases molecular diffusion, shortening the incubation time to minutes. Additionally, the microfluidic device eliminates the need for conventional lab procedures, enabling an automated assay. A mixing module fabricated with optimized geometry and herringbone structures is incorporated inside the mixing channel to achieve rapid and continuous mixing performance of reagents and samples (Figure 3.3A-i).

In order to determine the optimum injection flow rate, the competitive ELISA of MC-LR was performed in the devices. A syringe pump was utilized to inject the solutions at different flow rates (5, 15, and 30 μL/min). A reagent sample consisting of magnetic beads functionalized with MC-LR toxin ($\approx 10^5$ bead/ml) and MC-LR mcAb (1 μg/ml) was introduced through the reagent inlet while a buffer solution containing MC-LR was injected via the sample inlet. The beads were collected from the module outlet, washed, and incubated with the pAb-QDs for 1.5 hours on the benchtop. Applying the identical standard benchtop incubation in the second step for all solutions enables us to correlate the difference in the results to the different conditions of flow rates in the first incubation step. Next, the labelled beads were injected into a chamber, retained by a magnet, and fluorescence images were captured using a microscope. A comparison of the fluorescence signals at different flow rates confirm the previously chosen optimum flow rate (see Chapter 2), 15 μL/min, produced the maximum difference in fluorescence signal related to low and high concentrations of MC-LR (Figure 3.3A-ii). The residual time and the agitation inside the channel are two important factors in determining the optimized condition. At lower flow rates, residual time increases, but the agitation is unlikely to happen, which leads to the generation of a low fluorescence signal and a long incubation time. At higher flow rates, the flow is more agitated, while the reagent and sample spend less time in the channel, hindering the sufficient binding[71].

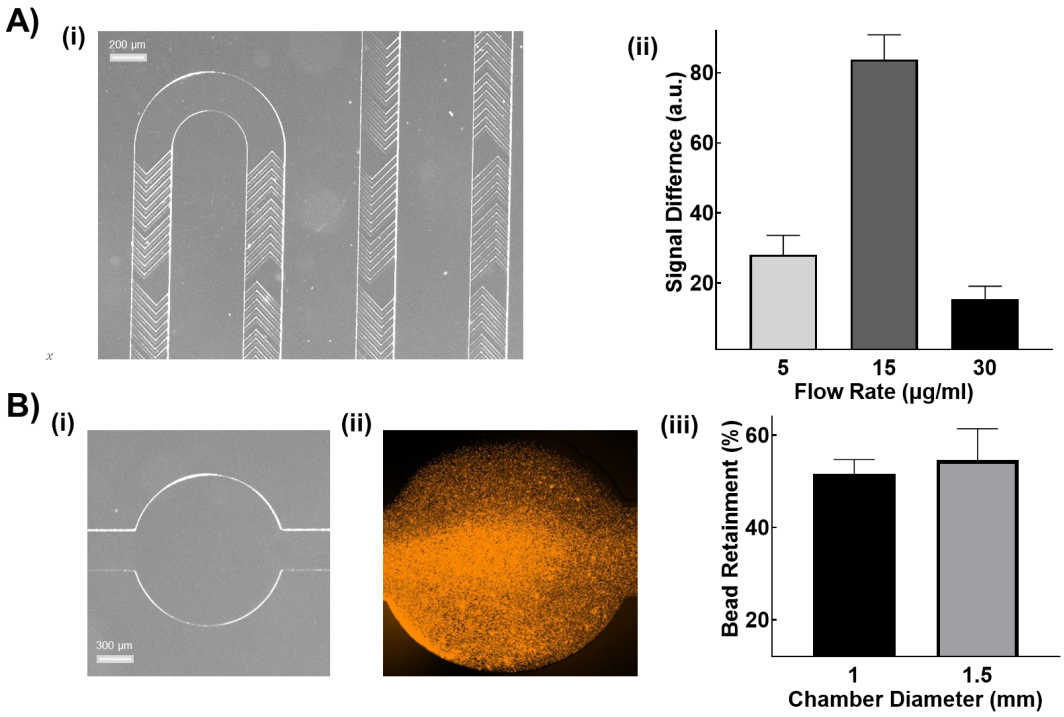

Figure 3.3: (A) i. Microscopic image of herringbone structured serpentine channel. The grooves are the herringbone layer of the channel. ii. Comparison of fluorescence signal in 0 and 1 μg/ml MC-LR at different flow rates. (B) i. Microscopic image of the circular detection chamber. ii. Microscopic images of retained fluorescence magnetic beads inside the channel. iii. Comparison of retainment of total injected beads inside the microfluidic device in two different diameters.

3.2.2 Fabrication and Optimization of the Detection Chamber

After the mixing and reactions took place inside the mixing module, the magnetic beads entered a chamber where it was possible to retain them magnetically. Several designs were put to the test in order to determine the best one for our objectives. The detection chamber should be a geometrical shape along the channel length to facilitate the retainment of beads by mitigating the drag force via increased cross-section and providing a defined region of interest for imaging. Another consideration is to avoid creating dead volume to minimize entrapment of the detection probes, which can lead to a high background signal. Based on these two observations, we decided on the circular shape for our chamber (Figure 3.3B-i). Next, we needed to find an optimum size for the circular chamber. Circular chambers of

0.5, 1, 1.5, and 2.5 mm diameter were fabricated and tested. The 0.5 mm diameter was ineffective as it was small and close to the microchannel width (0.3 mm). On the other hand, the 2.5 mm chamber was not functional as it collapsed.

The results in Figure 3.3B-iii (see Methods) indicate that the chamber size of 1.5 mm is more efficient in bead retainment, and the microscopic images (Figure 3.3B-ii) confirm that a dense bead pallet formed with this size. The magnetic force needs to be stronger than the drag force of the beads in the chamber in order to retain them. A bigger size chamber results in lower linear velocity (lower drag force), which could easily be prevailed by the magnetic power, resulting in a higher retainment ratio that is favourable. Therefore, the best results were obtained with a single circular chamber with optimal diameter of 1.5 mm. For immobilizing the beads, cylindrical magnets that matched the size of the chamber were utilized to create a powerful magnetic field.

3.2.3 Fabrication and Optimization of the Integrated Microfluidic Device

Next, under the shed of the previous experiences with mixing modules and detection chambers, a new integrated device was designed and fabricated containing both modules. The new device brought our design a step closer to total automation as the outlet of the mixing module was directly connected to the collection chamber. We used a syringe pump to inject the target sample and reagent solution into the device through the two inlets with the optimized flow rate. During the analysis of the Toxin Chip, the two flows were mixed and reacted in the mixing module and then entered the detection chamber, where the beads were retained, and the second incubation step was performed (see Methods). Following incubation, the chamber was washed with a washing buffer to remove any remaining unbound pAb-QDs.

The second incubation step of the toxin chip needs to be optimized. During this incubation, the pAb-QDs solution was introduced at a low flow rate (15 μL/h) into the collection chamber to label the immunocomplex on the surface of the beads for the subsequent detection step under a fluorescent microscope. The incubation time of pAb-QDs was investigated at 15, 30, and 60 minutes at the concentration of 10 μg/ml, where 30 minutes proved to be the optimum incubation time for MC-LR detection (Figure 3.4A-i). Similarly, 5 μg/ml was determined as an optimum concentration for pAb-QDs solution during the experiment with three different concentrations of 1, 5, and 10 μg/ml at the 30 minutes incubation (Figure 3.4A-ii). A comparison of the fluorescence signals obtained under these conditions showed that the 5 μg/ml and 30 minutes incubation time for pAb-

QDs resulted in the highest fluorescence signal (Figure 3.4A), and the significant difference between fluorescence signals of 0 and 1 μg/ml of MC-LR (Figure 3.4A and Figure A.7).

3.3 Image Recognition Platform

We developed a custom program to measure the fluorescence signal intensity and quantify the toxin concentrations. This program automatically calculates the concentration of the target toxin based on the fluorescence signal and embedded calibration functions. Many fluorescence images were utilized for training the program and determining an applicable light intensity range to extract the mean fluorescence intensity of the collected beads inside the detection chamber (Figure 3.4B). Threshold values were determined to exclude the background areas around the beads and the excessively bright fluorescence spots from the measurement. These bright spots could be formed due to the agglomeration and entrapment of pAb-QDs that the washing step was not able to remove. Figure 3.4B-top shows histogram of an image of detection chamber with a high fluorescence signal intensity, the light intensity distribution shifted to the right, representing a high light intensity of collected beads. In contrast, for an image with the lower fluorescence signal intensity (Figure 3.4B-bottom), the distribution shifts to the left indicating a low light intensity of beads.

3.4 Detection of MC-LR and OA Using Toxin-Chip

We then utilized the optimized conditions obtained for mcAb and pAb-QDs concentrations, mixing device flow rate, the incubation time inside the detection chamber, and the image analysis program to develop the calibration curves for MC-LR and OA. Water samples were spiked with different concentrations of toxin and injected into the microfluidic platform. The incubation steps were performed on the device, and the captured fluorescence images were analyzed using the developed program. A decrease in the fluorescence signals emitted from collected beads by increasing toxin concentrations was observed. Using our device, toxin levels can be measured within 45 mins. Using these measurements, calibration curves were constructed that correlate the fluorescence signal intensity with toxin concentration for MC-LR (Figure 3.5A) and OA (Figure 3.5B). Our device achieved a LOD of 9.7×10^{-5} μg/ml for MC-LR and 3.7×10^{-5} μg/ml for OA (see Methods). These LODs are very below the recommended concentration of these toxins as a safety guideline for drinking

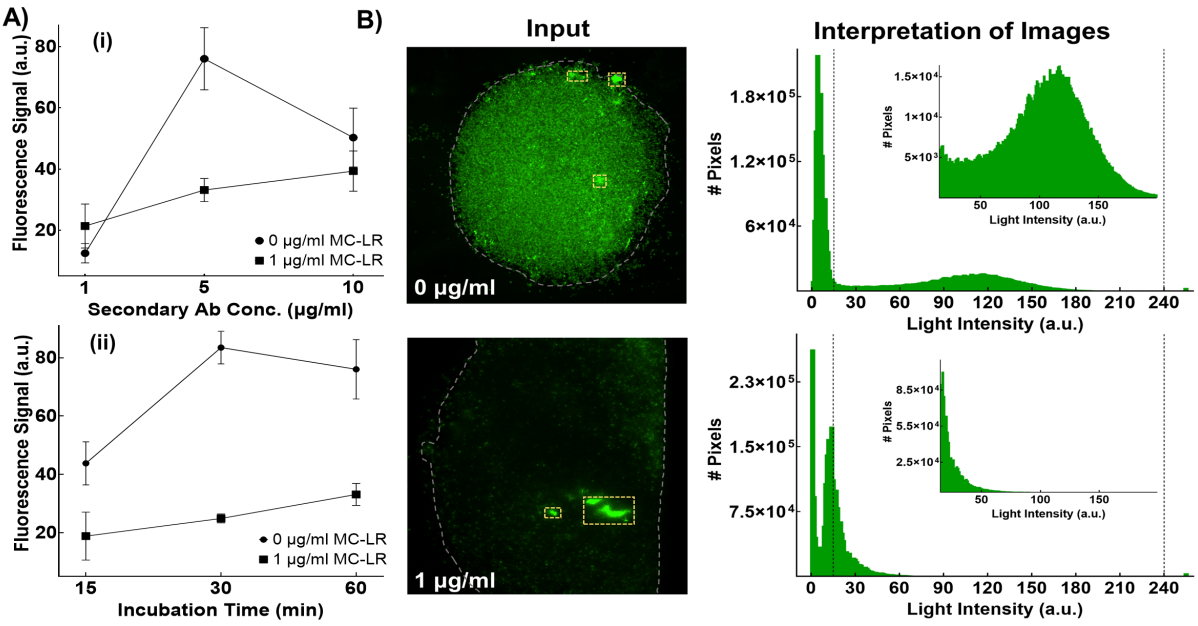

Figure 3.4: (A) Optimization of second incubation step on Toxin-Chip. Investigation of incubation time (i) and pAb-QDs concentration (ii) effect on the measured fluorescence signal in the analysis of 0 and 1 μg/ml of MC-LR. (B) Microscopic image analysis using the image analysis program. The fluorescence image was divided into pixels, and the light intensity of each pixel was measured. The results were represented in the histogram graphs reporting number of pixels (y-axis) vs light intensity (x-axis). The pixels of low light intensity (black areas) and high light intensity (highly fluorescence areas) were identified (dash lines in the histograms) and excluded from the calculation. Exclusion of the low and high light intensity boundaries results in a clearer and comparable histogram (inset in histogram graphs).

water which is 10^{-3} μg/ml. Therefore, our microfluidic platform can achieve sufficient sensitivity to measure safety-relevant concentrations of MC-LR and OA.

3.5 Selectivity of the Assay

We next studied the selectivity of our assay for specific toxin detection. Water samples are a complex sample matrix and include many molecules that can potentially interfere with the detection assay. Selectivity of the assay toward the target of interest is crucial

in determining the accuracy of new sensing technology. The presented immunoassay utilizes antibodies as a recognition element that is selective toward the target toxin. The Toxin-Chip was tested for its ability to detect a specific toxin in the presence of interfering species commonly present in freshwaters. It displayed remarkable specificity against interferents, including CYN and STX. These interferences are purposefully selected as CYN is a freshwater toxin like MC-LR, and STX is a marine toxin similar to OA. During this investigation, interferences did not affect the assay in a low or high concentration of the target of interest (Figure 3.5C, D), and possible cross-reactivity was avoided. As a result, we conclude that the detection assay is highly specific to the targeted toxin and robust to various interferences.

We next studied the stability of the bead-bound immunocomplex and pAb-QDs for 0.0001 ug/mL of MC-LR by monitoring the fluorescence signal of beads over three weeks (Figure A.6). In this experiment, the beads from the benchtop experiment are retained in the chamber and stored in a cold and dark place to measure the fluorescence signal change. We observed about 12.5%, 23%, and 28.5% drop in the measured signal after 3 days, 10 days, and 3 weeks, respectively. This observation proves the immunocomplex and QDs signal stability, verifying the assay robustness.

We have then evaluated the Toxin-Chip capability for simultaneous detection of two toxins. The multiplexed device was designed and fabricated considering the optimized geometry (Figure 3.6A). Defined concentrations of MC-LR and OA were spiked into a buffer solution and injected into the device through the sample inlet. The MC-LR and OA reagent solutions were prepared and introduced to the mixing microfluidic device through their specific reagent inlets. We tested the multiplexity of the device using four samples: 1) a blank solution with no toxins, 2) a MC-LR solution with no OA, 3) an OA solution with no MC-LR, and 4) a solution with both MC-LR and OA. Figure 3.6B shows the microscopic images of two detection chambers corresponded to the four conditions. With the introduction of the first solution, a high fluorescence signal was observed in both chambers, which correlates to the zero concentration of toxin. The second and third samples resulted in a reduced fluorescence signal in MC-LR and OA detection chamber, respectively. These results indicate that the reagents are only responsive to their toxin target, confirming no cross-reactivity in the assay. Introducing the fourth solution led to a reduced fluorescence signal in both MC-LR and OA detection chamber. This observation confirms the capability of the Toxin-Chip for multiplexed and simultaneous detection of MC-LR and OA in a single run.

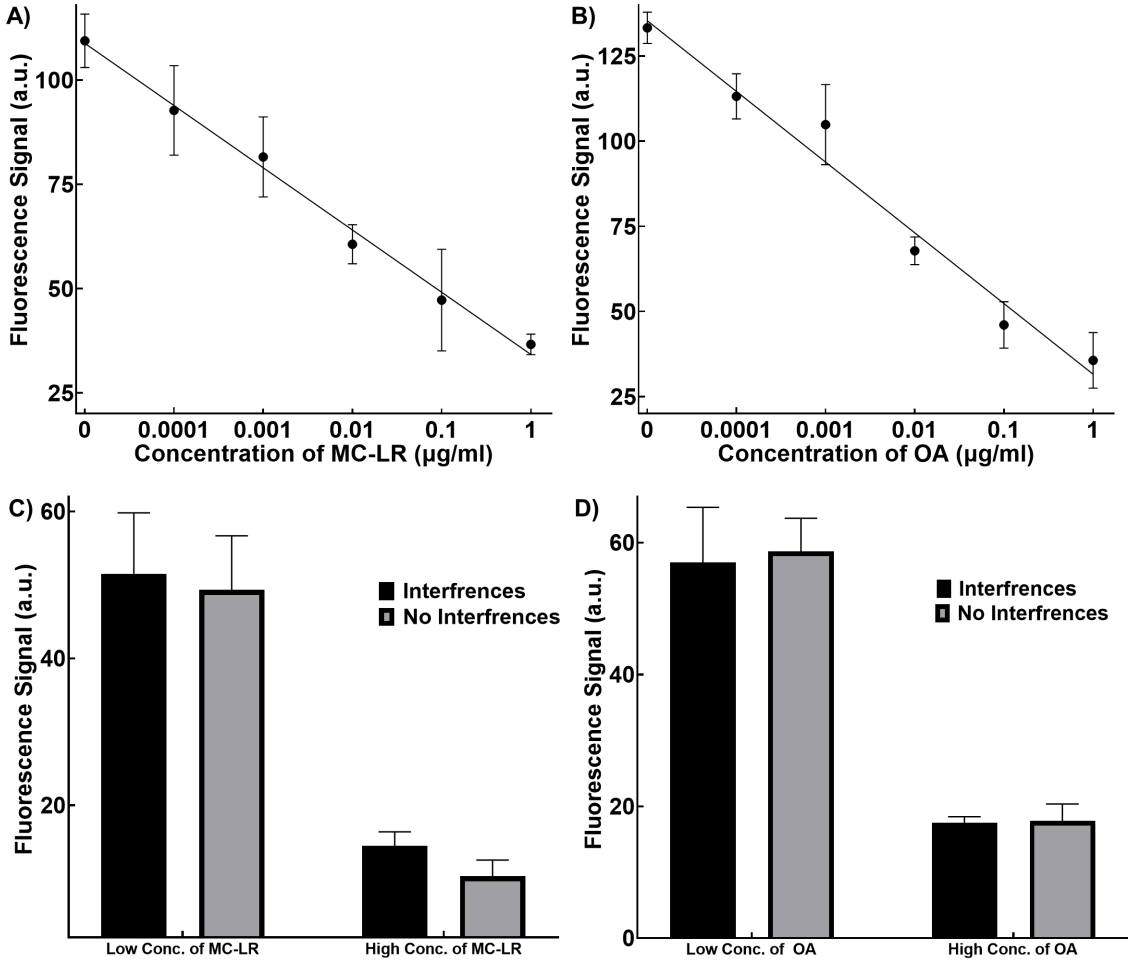

Figure 3.5: The calibration curve of quantification of MC-LR ($R^2 = 0.93$) (A) and OA ($R^2 = 0.96$) (B) with Toxin-Chip. B) Investigation performance of MC-LR assay (C) and OA assay (D) in the presence of interference, CYN and STX with concentration of 1 μg/ml.

3.6 Detection of Toxin in the Lake Water

The field samples are more complex, and the presence of the interfering substances makes the analysis challenging. Due to the vital importance of in-field application for a toxin monitoring system, the Toxin chip was employed for the detection of spiked water samples. To assess the matrix effect on the analysis process, we collected water samples from Columbia Lake in Waterloo, Ontario, and spiked them with a stock solution of MC-LR

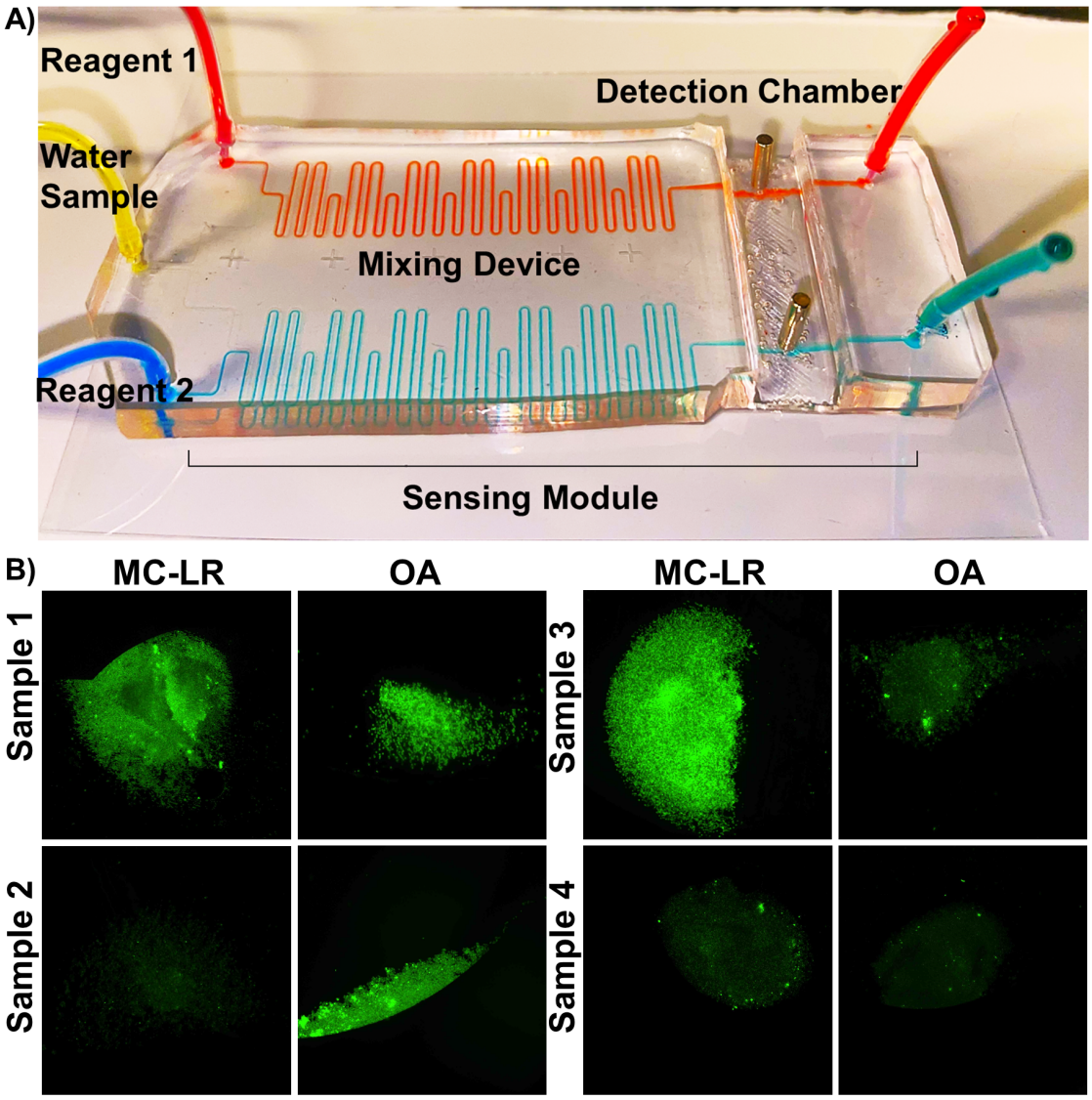

Figure 3.6: A) Fabricated Toxin-Chip, the sample inlet (represented with yellow color) is divided and mixed with two specific reagents (represented with blue and red colors). B) Microscopic images of the beads retained inside two detection chambers. The fluorescence signal is reduced in response to the existence of the target toxin in the inlet sample. The images confirm the simultaneous detection of two toxins in Toxin-Chip

and OA. Table 3.1 shows the toxin recoveries, which were computed as the ratio of the detected concentrations to the spiked concentrations. The recoveries vary from 99% to 108%, demonstrating that the technique can effectively reduce the need for pre-treatment and can be used for real sample analysis. The low matrix effect was owing to the specificity of the antigen-antibody reaction, the large surface area of microbeads, and the amplification of signal by the magnetic collection of beads.

Table 3.1: Toxin detection from lake water samples

recovery (%)	**0 μg/ml**	**1 μg/ml**
MC-LR	99.46	107.97
OA	104.43	103.88

Chapter 4

Conclusion

We have developed a model to simulate the analyte–antibody reaction on the surface of moving beads inside a microfluidic channel. The model considers the effect of the channel geometry, flow rates, antibody and analyte concentrations, analyte diffusion, association rate, dissociation rate, external forces, and bead size and numbers. The results demonstrate the model's capability for simulating different conditions and its potential as an optimization tool in the microfluidic biosensors. Moreover, the comparison of simulation results with the experimental ones showed a good correlation and validated our model. We have also expanded our model by investigating the equilibrium inside the microfluidic device using a kinetic model.

Various studies have formulated and modeled the immunobead-based assay, but these studies are limited to a stable reaction environment and are not applicable to microfluidic devices. In the presented model, an active reaction environment is simulated that includes different movements in a continuous flow microfluidic device. The model can be adjusted for simulating other microfluidic related experiments such as magnetic retention of beads, dielectrophoretic separation, and ultrasound mixing. We believe that the model has the potential for further development to produce more precise results by considering the rotation of beads in the channel. Moreover, the beads' interaction and collision with the analyte affect the movement profiles in the channel as well as the capture rate. Considering these effects would make the model more robust and accurate.

In the next step, we employed the optimized channel design to develop a microfluidic biosensor to quantify toxins in water samples. Monitoring of toxins is becoming increasingly important considering their alarming expansion and potential dangers to human health. Here, we designed and fabricated a novel microfluidic platform capable of detecting two

types of toxin, MC-LR, a freshwater toxin, and OA, a marine toxin. For this purpose, a bead-based, indirect competitive ELISA was integrated with a specifically designed microfluidic system providing a sensitive, multiplex, and robust fluorescence-based sensor. Implementation of microbeads provides an efficient and flexible assay, whereas QDs' utilization as detection agents further enhance the sensitivity of the assay. The fluorescent signal emitted from beads was reversely proportional to the concentration of target toxins.

An image analysis program was also developed to automate the measurement and quantification of the fluorescence signal from microscopic images of beads. The Toxin-Chip yielded a high analytical performance of 1-10 $\times$ 10^{-5} μg/L (LOD) with exceptionally excellent chemical stability over time and specificity against interfering toxins or other possible biomolecules in the lake water. We have designed and tested the device for simultaneous detection of MC-LR and OA. However, the Toxin-Chip can contain multiple sensing modules, allowing for the detection of more toxins.

We have compared our sensor with previously reported sensors for toxin detection (Table 4.1). The Toxin-Chip showed a comparable LOD and reaction time. Although the reusable sensor presented by zhang and co-workers[48] reports a low LOD and reaction time, their assay is complex that requires eight steps to complete. Given the multiplex capability and accuracy of the assay, as well as portability and cost-effectiveness, the integrated Toxin-Chip can be applied to monitor toxins and can be modified to detect other toxins in environmental water. The next steps are bench-marking the Toxin-Chip with conventional LC-MS methods using lake water samples containing intrinsic toxins. The future improvement is simplifying fluorescence image capture system by developing a portable optic system and developing a mobile app for image analysis. This will make the Toxin-Chip suitable for in-field analysis.

Table 4.1: Microfluidic fluorescent biosensors for toxin detection.

Method	**Targets**	**Range**	**LOD**	**Time (min)**	**Reusable**	**Ref.**
Indirect competitive ELISA on surface	MC-LR CYN	0.4–3.1 ng/mL 0.7–2.7 ng/mL	0.4 ng/mL 0.7 ng/mL	>30	No	[47]
Direct competitive ELISA on beads and in droplet	MC-LR	10^{-4}–100 ng/mL	1.2×10^{-5} ng/mL	>60	Yes	[49]
Direct competitive ELISA on bead	MC CYN STX	0.15–5.0 ng/ mL 0.05–2 ng/ mL 0.02–0.4 ng/ mL	0.02 ng/ mL 0.015 ng/ mL 0.02 ng/ mL	>30	Yes	[48]
Aptameric competitive assay	ATX CYN NOD MC-LR	2.3–1.6 $\times 10^4$ng/ mL 6.6–4.2 $\times 10^4$ ng/ mL 19–8.2 $\times 10^4$ ng/ mL 8–1 $\times 10^5$ ng/ mL	0.2 ng/ mL 0.8 ng/ mL 2.3 ng/ mL 1.4 ng/ mL	>10	No	[50]
Indirect competitive ELISA on bead	MC-LR OA	0.1 -1000 ng/mL	0.097 ng/mL 0.037 ng/mL	45	Yes	This work

Chapter 5

Material and Methods

5.1 Microfluidic Device

5.1.1 Material

For the fabrication of microfluidic devices, PDMS elastomer (Sylgard 184) was obtained from Dow Corning, and SU8-3050 and SU8-developer were received from Kayaku Advanced Material. The silicon wafer was purchased from University Wafer.

5.1.2 Fabrication Process

A standard microfluidic device fabrication protocol with glass substrates and PDMS was used to build the devices for experiments.The photomasks for the serpentine channel, bead retainment chamber, integrated detection devices, and herringbone structures were designed on AutoCAD software and then printed (CAD/Art Services). The masks were utilized for the fabrication of master molds on clean silicon wafers. A layer of SU8-3050 was spin-coated on the wafer to form a 45 μm thick layer. The wafer was then prebaked at 90 °C, exposed to UV light with a serpentine channel photomask (MA6 Mask Aligner, SUSS MicroTec, Germany), and developed by submerging in SU8-developer for 7 min. The single-layered molds were hard-baked at 150 °C to finalize the fabrication of the simple serpentine channel. The other serpentine channel and integrated detection devices mold was post baked at 90 °C to stabilize the channel structures, and then, the second layer of SU8 was cast in the same manner. The herringbone mask was aligned with the serpentine

channel structures on the mold with the help of a mask aligner. At last, the second layer was exposed and developed, completing the fabrication of the herringbone-structured serpentine channel. Overnight salinization was performed on fabricated mold in a vacuum desiccator. The PDMS and curing agent were mixed in a 10:1 ratio, and then, the air bubbles were removed using a desiccator. The PDMS polymer was poured onto the molds and heated at 70 °C in an oven for 2 h. The PDMS replicas were peeled off from the mold and cut into the desired shape. Inlets and outlet holes were punched in the PDMS replica for fluid injection. In the next step, the PDMS structures and cleaned glass slides were bound to each other with plasma treatment (Tergeo Plasma Cleaner, Pie Scientific). The punched inlets and outlets were connected to silicone tubing to complete the microfluidic device fabrication. Before use, the devices were degassed with Pluronic solution overnight.

5.1.3 Microfluidic Device Design

Mixing module

The channel with a total length of 35 cm and a cross-section of 300 μm $\times$ 45 μm was designed in a serpentine shape. The herringbone structures with a height of 45 μm were added to the top of the channel. The device has two inlets for sample and reagent injection and one outlet where the beads were collected.

Detection chamber

The circular chambers with diameters of 0.5, 1, 1.5, and 2.5 mm and an inlet and outlet channel with a length of 1 cm and a width of 300 μm were designed. The heigh of the design is 45 μm.

Integrated device

In a new design, the mixing module's outlet was connected to the detection chambers inlet to form the integrated device. As the outlet of the mixing module has a doubled linear velocity comparing the inlets (two inlets, one outlet), the width of the connection path between the two modules was gradually enlarged from 300 to 600 μm. The expanded width will balance off the increased linear velocity, resulting in the same flow rate. Similar to the mixing module, the device has two inlets for sample and reagent and one outlet.

5.2 Computational Study and COMSOL Simulation

The model was developed by customizing the COMSOL Multiphysics software program (License purchased from CMC Microsystems). A COMSOL model was developed to study

the analyte movements inside a channel and the reaction at the surface of beads and customized to overcome the limitations of modeling a moving item (e.g., bead) inside the channel. The laminar flow physics was utilized to simulate the advection and diffusion of the analyte in the designed microfluidic channel. The time-dependent location of the analytes allows the calculation of binding reaction on the surface of beads. This data was then transferred to the next model (capture model) where an element is defined inside the channel (bead and a defined space around it), and antigens entering this element are influenced by the reaction happening on the bead's surface. The chemistry of binding reaction on a reactive surface (bead) is simulated in the capture model by Chemistry, Transport of Diluted Species, and Surface Reaction packages. Briefly, the model simulates analyte movements in the capture circle and reports the surface concentration of the analyte on the bead(s) by time.

5.3 Analytical Measurements

5.3.1 Flow Cytometry

The collected beads from the device outlet were immediately centrifuged to wash and avoid further incubation inside the collecting tube that can cause an error in the measurements. Two steps of washing were followed to prepare the beads for the flow cytometer measurements. The washed bead pellet was resuspended in 200 μL of buffer solution and transferred to FACS tubes. Data were acquired and analyzed with the NovoExpress software. Gating of beads was performed based on FCS/SSC parameters so that unbound molecules or other possible aggregates are excluded from the analysis. The number of beads and emitted fluorescence signal of gated beads was collected at the specific FITC channel (510–520 nm).

5.3.2 Fluorescent Microscope Imaging

The fluorescence signal caused by the presence of FITC or QDs on the beads was measured under an inverted microscope (ECLIPISE Ti2, Nikon, Japan)) after beads collection at the detection chamber. The samples were flowed into a circular chamber (d = 1.5 mm) with an optimized flow rate (15 μL/min). An external magnet was placed on top of the chamber to retain the magnetic beads. Bead's pellets were illuminated by the laser, which captures fluorescence intensity that indicates the amount of the target antigen in the solution.

5.4 Immunoassays

5.4.1 Material

Carboxylated Magnetic Beads (3 μm) and streptavidin-coated microspheres (4.5 and 8 μm) were obtained from Bangs Laboratories. The magnets were purchased from McMaster-Carr.

Native Human IgG protein and matched detection antibody with FITC tag were obtained from Abcam. The IgG capture antibody was purchased from Antibodies-online.

MC-LR toxin, BSA conjugated MC-LR, OA mcAb, and BSA conjugated OA were obtained from Creative Diagnostics. The MC-LR mcAb was purchased from Enzo Life Sciences. OA toxin provided by MilliporeSigma, and CYN and STX were obtained from Eurofins.

5.4.2 Benchtop Assay - Indirect Competitive Assay of Toxin

irst, the carboxylated magnetic beads were incubated with EDC and NHS (1:1) for 30 min in MES buffer to activate the carboxylic groups on the surface of the bead. Next, the activated beads were functionalized with toxin-BSA for 3-4 hours. At last, the surface of the beads was blocked by incubating the with glycine solution to avoid any unwanted conjugation. In the first step of the assay, the toxin-bound beads were incubated with mcAb and target toxins for 1.5 hours. Then, the beads were washed and incubated with pAb-QDs (1:50) for another 1.5 hours. Finally, the beads were washed, and the fluorescence signal was measured by observing beads under the microscope (ECLIP-ISE Ti2, Nikon, Japan) (Figure A.5).

5.4.3 Microfluidic Device Assay - Sandwich assay of IgG

Two immunoreactions take place inside the microfluidic channel and form the sandwich molecules on the bead. The reactions are between IgG and the cAbs-conjugated beads and between dAbs and the captured IgG. In our experiments, both reactions take place simultaneously inside the mixing module. First, the biotinylated IgG cAbs were conjugated on the streptavidin coated beads. In this step, the beads were mixed with antibodies and placed in a shaker incubator for 1.5 h, allowing them to form biotin-streptavidin bound. We used a syringe pump to inject the target sample and reagent solution into the device

through two inlets with the defined flow rate. The injected reagent consists of cAbs-conjugated beads (4×10^5 beads/mL) and IgG dAbs (10 μg/mL), and the injected target sample is IgG (1 μg/mL). Two flows were mixed and reacted in the mixing module, and the beads were collected from the device outlet. The fluorescence signal of the beads then was measured using flow cytometry (NovoCyte, Agilent) or the fluorescence microscope.

5.5 Bead Retainment in the Chamber

The efficiency of the two diameters was evaluated with the optimized flow rate (15 μL/min) and fluorescence beads of the same size as the original beads. Some of the beads will settle in injection syringes, tubes, and channels, which yields a lower number of beads in the chamber. Therefore, we need to find the net amount of beads entering the chamber (B_n). The B_n was determined by injecting beads solution with a known number of beads (10^6) into the chamber without a magnet on top, and counting particles collected in the outlet. In the next step, the same experiment was repeated with the magnet on top of the chamber. By subtracting the B_n from the number of beads collected in the magnet experiment, the total retained beads (B_r) was calculated. Finally, the retainment ratio is equal to B_r divided by B_n.

5.6 Statistical Analysis

The LOD of toxin quantification was calculated with the help of calibration curves. First, we calculated the maximum distinguishable signal using the measured signal for blank (FL_b) and its standard deviation (SD_b) through equation 5.1. Then, we substituted the calculated (FL_m) in the calibration curve equations (5.2) to attain the related concentration. This concentration is the lowest concentration that the assay can measure.

$$FL_m = FL_b - 3 \times SD_b \tag{5.1}$$

$$\begin{cases} FL = 34.69 - 14.81 \times log(C) & R^2 = 0.93 \quad MC - LR \\ FL = 31.56 - 20.76 \times log(C) & R^2 = 0.96 \quad OA \end{cases} \tag{5.2}$$

The equivalence of spiked lake water and buffer solutions was tested using statistical analysis. To look for any significant differences between the two groups, we used the

Kruskal test. The p-values of the Kruskal test were higher than the significance level (0.32-0.38 ¿ 0.05), indicating that the measured fluorescence signal from the buffer and lake water solution were identical.

References

[1] Rajni Kaushik and Rajasekhar Balasubramanian. Methods and Approaches Used for Detection of Cyanotoxins in Environmental Samples: A Review. *Critical Reviews in Environmental Science and Technology*, 43(13):1349–1383, 1 2013.

[2] Meng Liu, Huimin Zhao, Shuo Chen, Hongtao Yu, and Xie Quan. Colloidal Graphene as a Transducer in Homogeneous Fluorescence-Based Immunosensor for Rapid and Sensitive Analysis of Microcystin-LR. *Environmental Science & Technology*, 46(22):12567–12574, 2012.

[3] Chunlong Zhang and Jianying Zhang. Current Techniques for Detecting and Monitoring Algal Toxins and Causative Harmful Algal Blooms. *Journal of environmental analytical chemistry*, 2015, 2014.

[4] Karishma Shah and Panagiotis Maghsoudlou. Enzyme-linked immunosorbent assay (ELISA): the basics. *British Journal of Hospital Medicine*, 77(7):C98–C101, 7 2016.

[5] C T Lim and Y Zhang. Bead-based microfluidic immunoassays: The next generation. *Biosensors and Bioelectronics*, 22(7):1197–1204, 2007.

[6] H Cumhur Tekin and Martin A M Gijs. Ultrasensitive protein detection: a case for microfluidic magnetic bead-based assays. *Lab on a Chip*, 13(24):4711–4739, 2013.

[7] Luciano F Huergo, Khaled A Selim, Marcelo S Conzentino, Edileusa C M Gerhardt, Adrian R S Santos, Berenike Wagner, Janette T Alford, Nelli Deobald, Fabio O Pedrosa, Emanuel M de Souza, Meri B Nogueira, Sônia M Raboni, Dênio Souto, Fabiane G M Rego, Dalila L Zanette, Mateus N Aoki, Jeanine M Nardin, Bruna Fornazari, Hugo M P Morales, Vânia A Borges, Annika Nelde, Juliane S Walz, Matthias Becker, Nicole Schneiderhan-Marra, Ulrich Rothbauer, Rodrigo A Reis, and Karl Forchhammer. Magnetic Bead-Based Immunoassay Allows Rapid, Inexpensive, and Quantitative Detection of Human SARS-CoV-2 Antibodies. *ACS Sensors*, 6(3):703–708, 2021.

[8] Águeda Molinero-Fernández, María Moreno-Guzmán, Miguel Ángel López, and Alberto Escarpa. Magnetic Bead-Based Electrochemical Immunoassays On-Drop and On-Chip for Procalcitonin Determination: Disposable Tools for Clinical Sepsis Diagnosis. *Biosensors*, 10(6):66, 2020.

[9] Sung-Yi Yang, Kang-Yi Lien, Kao-Jean Huang, Huan-Yao Lei, and Gwo-Bin Lee. Micro flow cytometry utilizing a magnetic bead-based immunoassay for rapid virus detection. *Biosensors and Bioelectronics*, 24(4):855–862, 2008.

[10] Eric Rogier, Mateusz Plucinski, Naomi Lucchi, Kimberly Mace, Michelle Chang, Jean Frantz Lemoine, Baltazar Candrinho, James Colborn, Rafael Dimbu, Filomeno Fortes, Venkatachalam Udhayakumar, and John Barnwell. Bead-based immunoassay allows sub-picogram detection of histidine-rich protein 2 from Plasmodium falciparum and estimates reliability of malaria rapid diagnostic tests. *PLOS ONE*, 12(2):e0172139, 2017.

[11] Elieser Gorelik, Douglas P Landsittel, Adele M Marrangoni, Francesmary Modugno, Lyudmila Velikokhatnaya, Matthew T Winans, William L Bigbee, Ronald B Herberman, and Anna E Lokshin. Multiplexed Immunobead-Based Cytokine Profiling for Early Detection of Ovarian Cancer. *Cancer Epidemiology Biomarkers & Prevention*, 14(4):981, 2005.

[12] Yi-Sin Chen, Yu-Dong Ma, Chihchen Chen, Shu-Chu Shiesh, and Gwo-Bin Lee. An integrated microfluidic system for on-chip enrichment and quantification of circulating extracellular vesicles from whole blood. *Lab on a Chip*, 19(19):3305–3315, 2019.

[13] Jazib Irfan, Ali Raza, and Muhammad Ali. Biosensors: Their Fundamentals, Designs, Types and Most Recent Impactful Applications: A Review. 1 2017.

[14] Ruben R G Soares, Felix Neumann, Catarina R F Caneira, Narayanan Madaboosi, Sibel Ciftci, Iván Hernández-Neuta, Inês F Pinto, Denis R Santos, Virginia Chu, Aman Russom, João P Conde, and Mats Nilsson. Silica bead-based microfluidic device with integrated photodiodes for the rapid capture and detection of rolling circle amplification products in the femtomolar range. *Biosensors and Bioelectronics*, 128:68–75, 2019.

[15] Dan Sun, Fanghao Cao, Weiqing Xu, Qidan Chen, Wei Shi, and Shuping Xu. Ultrasensitive and Simultaneous Detection of Two Cytokines Secreted by Single Cell in Microfluidic Droplets via Magnetic-Field Amplified SERS. *Analytical Chemistry*, 91(3):2551–2558, 2 2019.

[16] Bidhan Chandra Dhar and Nae Yoon Lee. Lab-on-a-Chip Technology for Environmental Monitoring of Microorganisms. *BioChip Journal*, 12(3):173–183, 2018.

[17] Terence G Henares, Shun-ichi Funano, Shigeru Terabe, Fumio Mizutani, Ryuichi Sekizawa, and Hideaki Hisamoto. Multiple enzyme linked immunosorbent assay system on a capillary-assembled microchip integrating valving and immuno-reaction functions. *Analytica Chimica Acta*, 589(2):173–179, 2007.

[18] Kiichi Sato, Manabu Tokeshi, Tamao Odake, Hiroko Kimura, Takeshi Ooi, Masayuki Nakao, and Takehiko Kitamori. Integration of an Immunosorbent Assay System: Analysis of Secretory Human Immunoglobulin A on Polystyrene Beads in a Microchip. *Analytical Chemistry*, 72(6):1144–1147, 3 2000.

[19] Kevin Ward and Z Hugh Fan. Mixing in microfluidic devices and enhancement methods. *Journal of micromechanics and microengineering : structures, devices, and systems*, 25(9):94001, 2015.

[20] Mahla Poudineh, Caitlin L Maikawa, Eric Yue Ma, Jing Pan, Dan Mamerow, Yan Hang, Sam W Baker, Ahmad Beirami, Alex Yoshikawa, Michael Eisenstein, Seung Kim, Jelena Vučković, Eric A Appel, and H Tom Soh. A fluorescence sandwich immunoassay for the real-time continuous detection of glucose and insulin in live animals. *Nature Biomedical Engineering*, 5(1):53–63, 2021.

[21] Thomas Gervais and Klavs F Jensen. Mass transport and surface reactions in microfluidic systems. *Chemical Engineering Science*, 61(4):1102–1121, 2006.

[22] Todd M Squires, Robert J Messinger, and Scott R Manalis. Making it stick: convection, reaction and diffusion in surface-based biosensors. *Nature Biotechnology*, 26(4):417–426, 2008.

[23] Lei Chang, David M Rissin, David R Fournier, Tomasz Piech, Purvish P Patel, David H Wilson, and David C Duffy. Single molecule enzyme-linked immunosorbent assays: Theoretical considerations. *Journal of Immunological Methods*, 378(1):102–115, 2012.

[24] Lewis Roberts, Thom Griffith, Alan Champneys, Martina Piano, Janice Kiely, and Richard Luxton. Mathematical modelling of a magnetic immunoassay. *IMA Journal of Applied Mathematics*, 82(6):1253–1282, 2017.

[25] R Nooney D. Mackey E. Kelly. Modelling random antibody adsorption and immunoassay activity. *Mathematical Biosciences & Engineering*, 13(6):1159–1168, 2016.

[26] Bedabrata Saha, Toon H Evers, and Menno W J Prins. How Antibody Surface Coverage on Nanoparticles Determines the Activity and Kinetics of Antigen Capturing for Biosensing. *Analytical Chemistry*, 86(16):8158–8166, 2014.

[27] Ahsan Munir, Jianlong Wang, Zanzan Zhu, and H Susan Zhou. Residence time distribution analysis of magnetic nanoparticle-enhanced mixing using time-dependent magnetic actuation in microfluidic system. *Microfluidics and Nanofluidics*, 10(4):735–747, 2011.

[28] Dan Wu and Joel Voldman. An integrated model for bead-based immunoassays. *Biosensors and Bioelectronics*, 154:112070, 2020.

[29] Giliane Zanchett and Eduardo C Oliveira-Filho. Cyanobacteria and Cyanotoxins: From Impacts on Aquatic Ecosystems and Human Health to Anticarcinogenic Effects. *Toxins*, 5(10):1896–1917, 2013.

[30] Liting Qin, Yulong Gao, Wei Ni, Meiyu Sun, Yongqiang Wang, Chunhong Yin, Xiaole Qi, Honglei Gao, and Xiaomei Wang. Development and application of real-time PCR for detection of subgroup J avian leukosis virus. *Journal of clinical microbiology*, 51(1):149–154, 1 2013.

[31] J Zhang and C Zhang. Sampling and sampling strategies for environmental analysis. *International Journal of Environmental Analytical Chemistry*, 92(4):466–478, 4 2012.

[32] R M Dawson. the toxicology of microcystins. *Toxicon*, 36(7):953–962, 1998.

[33] Maria Prado-Alvarez, Fernanda Flórez-Barrós, Josefina Méndez, and Juan Fernandez-Tajes. Effect of okadaic acid on carpet shell clam (Ruditapes decussatus) haemocytes by in vitro exposure and harmful algal bloom simulation assays. *Cell Biology and Toxicology*, 29(3):189–197, 2013.

[34] Lionel Ho, Gretchen Onstad, Urs von Gunten, Stéphanie Rinck-Pfeiffer, Keith Craig, and Gayle Newcombe. Differences in the chlorine reactivity of four microcystin analogues. *Water Research*, 40(6):1200–1209, 2006.

[35] Revisions to the Unregulated Contaminant Monitoring Rule (UCMR 4) for Public Water Systems and Announcement of a Public Meeting. Technical report, 1 2019.

[36] Rie Nishiwaki-Matsushima, Tetsuya Ohta, Shinji Nishiwaki, Masami Suganuma, Kiyomi Kohyama, Takatoshi Ishikawa, Wayne W Carmichael, and Hirota Fujiki. Liver tumor promotion by the cyanobacterial cyclic peptide toxin microcystin-LR. *Journal of Cancer Research and Clinical Oncology*, 118(6):420–424, 1992.

[37] M Suganuma, H Fujiki, H Suguri, S Yoshizawa, M Hirota, M Nakayasu, M Ojika, K Wakamatsu, K Yamada, and T Sugimura. Okadaic acid: an additional non-phorbol-12-tetradecanoate-13-acetate-type tumor promoter. *Proceedings of the National Academy of Sciences of the United States of America*, 85(6):1768–1771, 3 1988.

[38] World Health Organization (WHO). Guidelines for drinking-water quality. 2004.

[39] U.S. Environmental Protection Agency Office of Water. Drinking Water Health Advisory for the Cyanobacterial Microcystin Toxins. 6 2015.

[40] European Food Safety Authority (EFSA). Marine biotoxins in shellfish - okadaic acid and analogues - Scientific Opinion of the Panel on Contaminants in the Food chain. *EFSA Journal*, 6(1):589, 1 2008.

[41] Qin Wei, Yanfang Zhao, Bin Du, Dan Wu, Yanyan Cai, Kexia Mao, He Li, and Caixia Xu. Nanoporous PtRu Alloy Enhanced Nonenzymatic Immunosensor for Ultrasensitive Detection of Microcystin-LR. *Advanced Functional Materials*, 21(21):4193–4198, 2011.

[42] Wei Zhang, Baoping Jia, and Hiroaki Furumai. Fabrication of graphene film composite electrochemical biosensor as a pre-screening algal toxin detection tool in the event of water contamination. *Scientific Reports*, 8(1):10686, 2018.

[43] Liping Zhou, Anna Zhu, Xuening Lou, Dan Song, Rong Yang, Hanchang Shi, and Feng Long. Universal quantum dot-based sandwich-like immunoassay strategy for rapid and ultrasensitive detection of small molecules using portable and reusable optofluidic nano-biosensing platform. *Analytica Chimica Acta*, 905:140–148, 2016.

[44] L A Bentolila. 5 - Photoluminescent quantum dots in imaging, diagnostics and therapy. In Michael R Hamblin and Pinar Avci, editors, *Applications of Nanoscience in Photomedicine*, pages 77–104. Chandos Publishing, Oxford, 2015.

[45] Yanli Zhang, Zhenyu Zhu, Xia Teng, Yanqiong Lai, Shaofu Pu, Pengfei Pang, Hongbin Wang, Chun Yang, Colin J. Barrow, and Wenrong Yang. Enzyme-free fluorescent detection of microcystin-LR using hairpin DNA-templated copper nanoclusters as signal indicator. *Talanta*, 202, 2019.

[46] Shijia Wu, Nuo Duan, Hui Zhang, and Zhouping Wang. Simultaneous detection of microcysin-LR and okadaic acid using a dual fluorescence resonance energy transfer aptasensor. *Analytical and Bioanalytical Chemistry*, 407(5):1303–1312, 2015.

[47] Sarah R Bickman, Katrina Campbell, Christopher Elliott, Caroline Murphy, Richard O'Kennedy, Philip Papst, and Michael J Lochhead. An Innovative Portable Biosensor System for the Rapid Detection of Freshwater Cyanobacterial Algal Bloom Toxins. *Environmental Science & Technology*, 52(20):11691–11698, 2018.

[48] Jinling Zhang, Sixiu Liu, Pengyuan Yang, and Guodong Sui. Rapid detection ofalgal toxins by microfluidic immunoassay. *Lab on a Chip*, 11(20):3516–3522, 2011.

[49] Tian Guan, Jianfei He, Dayu Liu, Zaoqing Liang, Bowen Shu, Yiping Chen, Yingju Liu, Xing Shen, Xiangmei Li, Yuanming Sun, and Hongtao Lei. Open Surface Droplet Microfluidic Magnetosensor for Microcystin-LR Monitoring in Reservoir. *Analytical Chemistry*, 92(4):3409–3416, 2020.

[50] Zheng Li, Shengwei Zhang, Tao Yu, Zhiming Dai, and Qingshan Wei. Aptamer-Based Fluorescent Sensor Array for Multiplexed Detection of Cyanotoxins on a Smartphone. *Analytical Chemistry*, 91(16):10448–10457, 2019.

[51] Bing Liu, Di Zhang, Haibin Ni, Delong Wang, Liyong Jiang, Degang Fu, Xiaofeng Han, Chi Zhang, Hongyuan Chen, Zhongze Gu, and Xiangwei Zhao. Multiplex Analysis on a Single Porous Hydrogel Bead with Encoded SERS Nanotags. *ACS Applied Materials & Interfaces*, 10(1):21–26, 1 2018.

[52] Howard A Stone. Introduction to Fluid Dynamics for Microfluidic Flows. In Hakho Lee, Robert M Westervelt, and Donhee Ham, editors, *CMOS Biotechnology*, pages 5–30. Springer US, Boston, MA, 2007.

[53] Jun Zhang, Sheng Yan, Ronald Sluyter, Weihua Li, Gursel Alici, and Nam-Trung Nguyen. Inertial particle separation by differential equilibrium positions in a symmetrical serpentine micro-channel. *Scientific Reports*, 4(1):4527, 2014.

[54] Junchao Wang, Victor G J Rodgers, Philip Brisk, and William H Grover. MOPSA: A microfluidics-optimized particle simulation algorithm. *Biomicrofluidics*, 11(3):34121, 2017.

[55] Lisen Wang, Jente Lu, Steven A Marchenko, Edwin S Monuki, Lisa A Flanagan, and Abraham P Lee. Dual frequency dielectrophoresis with interdigitated sidewall electrodes for microfluidic flow-through separation of beads and cells. *ELECTROPHORESIS*, 30(5):782–791, 2009.

[56] Rustem F Ismagilov, Abraham D Stroock, Paul J A Kenis, George Whitesides, and Howard A Stone. Experimental and theoretical scaling laws for transverse diffusive

broadening in two-phase laminar flows in microchannels. *Applied Physics Letters*, 76(17):2376–2378, 2000.

[57] K Saha, F Bender, and E Gizeli. Comparative Study of IgG Binding to Proteins G and A: Nonequilibrium Kinetic and Binding Constant Determination with the Acoustic Waveguide Device. *Analytical Chemistry*, 75(4):835–842, 2003.

[58] Gerson R Aguirre, Vitaly Efremov, Maria Kitsara, and Jens Ducrée. Integrated micromixer for incubation and separation of cancer cells on a centrifugal platform using inertial and dean forces. *Microfluidics and Nanofluidics*, 18(3):513–526, 2015.

[59] Ali Asgar S Bhagat and Ian Papautsky. Enhancing particle dispersion in a passive planar micromixer using rectangular obstacles. *Journal of Micromechanics and Microengineering*, 18(8):85005, 2008.

[60] Mei He, Jennifer Crow, Marc Roth, Yong Zeng, and Andrew K Godwin. Integrated immunoisolation and protein analysis of circulating exosomes using microfluidic technology. *Lab on a Chip*, 14(19):3773–3780, 2014.

[61] Yao Lu, Menglun Zhang, Hongxiang Zhang, Jingze Huang, Zhan Wang, Zelin Yun, Yanyan Wang, Wei Pang, Xuexin Duan, and Hao Zhang. On-chip acoustic mixer integration of electro-microfluidics towards in-situ and efficient mixing in droplets. *Microfluidics and Nanofluidics*, 22(12):146, 2018.

[62] Marine Bezagu, Stellios Arseniyadis, Janine Cossy, Olivier Couture, Mickael Tanter, Fabrice Monti, and Patrick Tabeling. A fast and switchable microfluidic mixer based on ultrasound-induced vaporization of perfluorocarbon. *Lab on a Chip*, 15(9):2025–2029, 2015.

[63] Milad Abolhasani, Ali Oskooei, Anna Klinkova, Eugenia Kumacheva, and Axel Günther. Shaken, and stirred: oscillatory segmented flow for controlled size-evolution of colloidal nanomaterials. *Lab on a Chip*, 14(13):2309–2318, 2014.

[64] Terje Tofteberg, Maciej Skolimowski, Erik Andreassen, and Oliver Geschke. A novel passive micromixer: lamination in a planar channel system. *Microfluidics and Nanofluidics*, 8(2):209–215, 2010.

[65] Chia-Yen Lee, Wen-Teng Wang, Chan-Chiung Liu, and Lung-Ming Fu. Passive mixers in microfluidic systems: A review. *Chemical Engineering Journal*, 288:146–160, 2016.

[66] Shakhawat Hossain, Mubashshir A Ansari, Afzal Husain, and Kwang-Yong Kim. Analysis and optimization of a micromixer with a modified Tesla structure. *Chemical Engineering Journal*, 158(2):305–314, 2010.

[67] Stroock Abraham D, Dertinger Stephan K W, Ajdari Armand, Mezić Igor, Stone Howard A, and Whitesides George M. Chaotic Mixer for Microchannels. *Science*, 295(5555):647–651, 2002.

[68] Eszter L Tóth, Eszter G Holczer, Kristóf Iván, and Péter Fürjes. Optimized Simulation and Validation of Particle Advection in Asymmetric Staggered Herringbone Type Micromixers. *Micromachines*, 6(1):136–150, 2015.

[69] Helen Song, Michelle R Bringer, Joshua D Tice, Cory J Gerdts, and Rustem F Ismagilov. Experimental test of scaling of mixing by chaotic advection in droplets moving through microfluidic channels. *Applied physics letters*, 83(12):4664–4666, 2003.

[70] Sanbo Qin, Lu Cai, and Huan-Xiang Zhou. A method for computing association rate constants of atomistically represented proteins under macromolecular crowding. *Physical biology*, 9(6):66008, 2012.

[71] Hamid Aghamohammadi, Seied Ali Hosseini, Sanjana Srikant, Alexander Wong, and Mahla Poudineh. Computational and Experimental Model to Study Immunobead-Based Assays in Microfluidic Mixing Platforms. *Analytical Chemistry*, 94(4):2087–2098, 2022.

APPENDICES

Appendix A

Supplementary Information

A.1 Tables

Table A.1 lists the k_{on} and k_{off} for the main and the non-specific reactions in our simulation. The nonspecific reactions must have a lowerk_{on} and a higher k_{off} than the main reaction since we utilize antibodies that are highly selective toward the target analyte.

Table A.1: Association and dissociation constants of the main and non-specific reactions

Reactions	$k_{on}(1/M.s)$	$k_{off}(1/s)$
Main Reaction	3.3×10^{4}	2.9×10^{-4}
Non-specific Reaction 1	6.6×10^{3}	5.8×10^{-3}
Non-specific Reaction 2	3.3×10^{3}	2.9×10^{-3}
Non-specific Reaction 3	1.5×10^{4}	1.5×10^{-3}

A.2 Figures

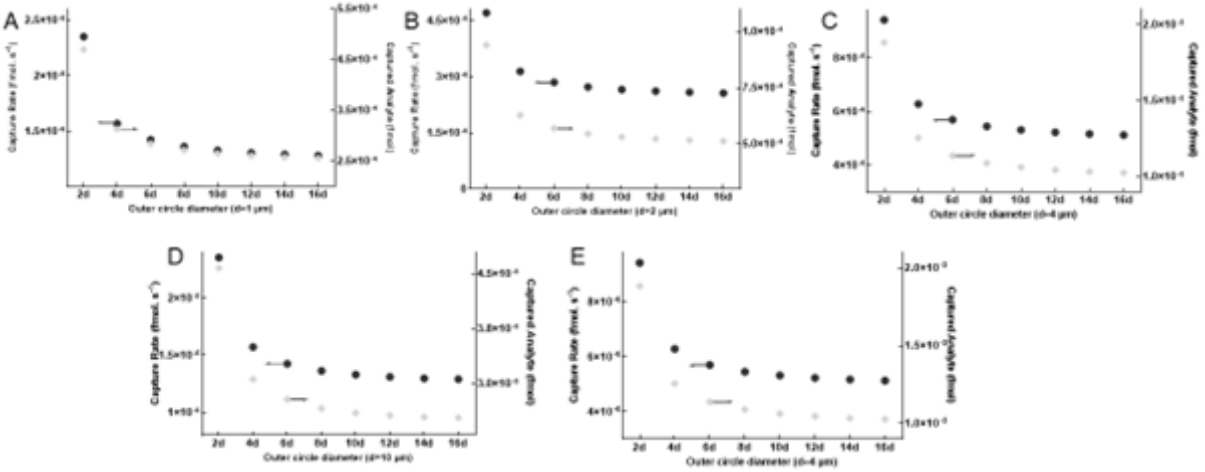

Figure A.1: Capture circle diameter analysis for different sizes of beads in a simple channel.

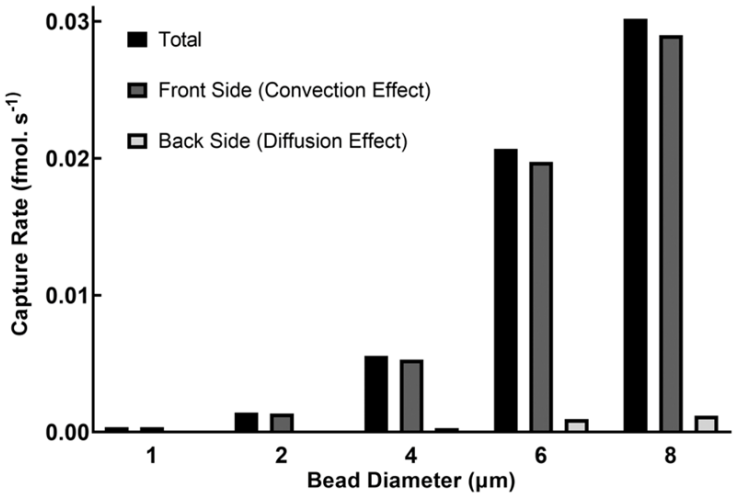

Figure A.2: Simulation results of capture rate on the total/front/back side of bead's surface for different sizes of bead.

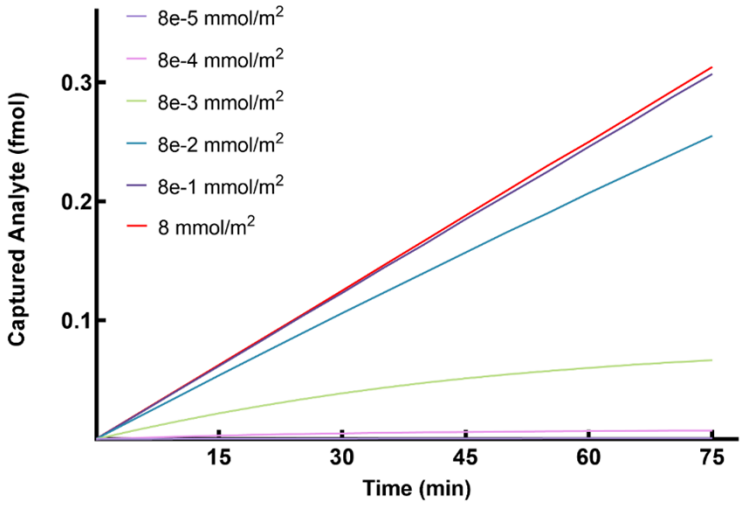

Figure A.3: Change of captured analyte concentration with increasing the concentration of antibody on the surface of bead.

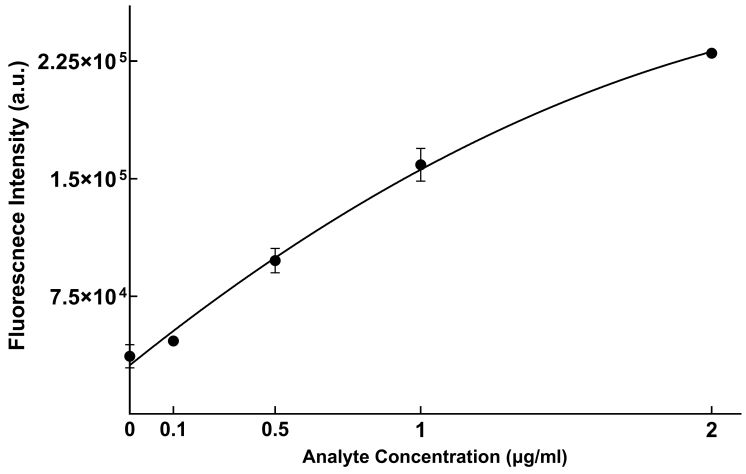

Figure A.4: Calibration curve of measured fluorescence signal vs analyte concentration.

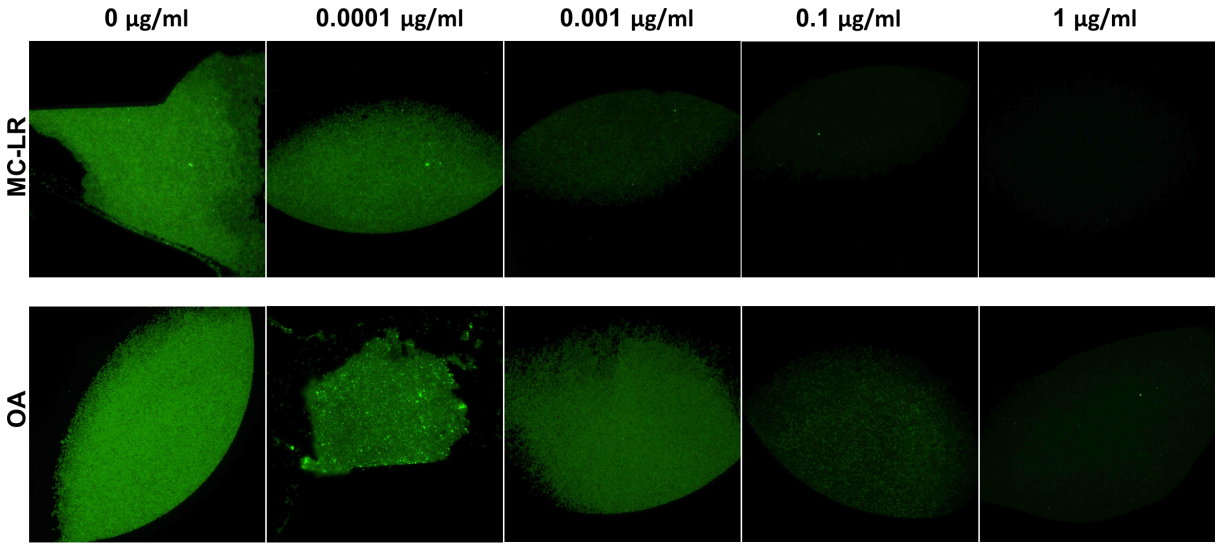

Figure A.5: Microscopic images of beads retained in the detection chamber in different concentrations MC-LR and OA.

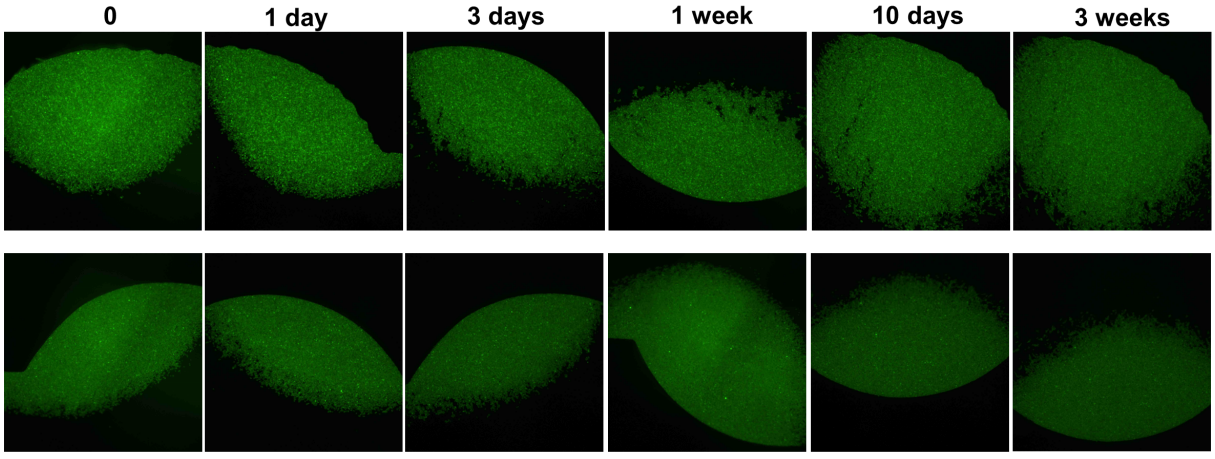

Figure A.6: Stability of fluorescence signal emitted from beads.

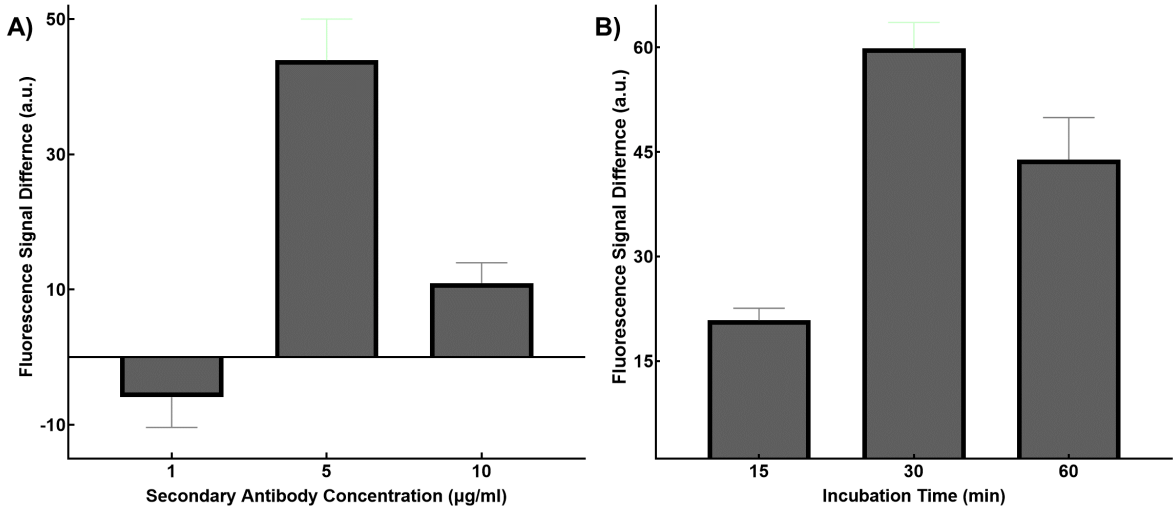

Figure A.7: Investigation of fluorescence signal range between the lowest (0 μg/ml) and the highest (1 μg/ml) concentration of MC-LR at different incubation times (A) and pAb-QDs concentration (B).